SNX10 functions as a modulator of piecemeal mitophagy and mitochondrial bioenergetics

Laura Trachsel-Moncho[1,2,3], Chiara Veroni[1,2,3#], Benan John Mathai[1,2,3#], Ana Lapao[1,2], Sakshi Singh[1,2], Nagham Theres Asp[1,2], Sebastian W. Schultz [2,3], Serhiy Pankiv[1,2], Anne Simonsen[1,2,3;*]

[1] Department of Molecular Medicine, Institute of Basic Medical Sciences Faculty of Medicine, University of Oslo, 1112 Blindern, Oslo 0317, Norway

[2] Centre for Cancer Cell Reprogramming, Institute of Clinical Medicine, Faculty of Medicine, University of Oslo, Oslo, Norway

[3] Department of Molecular Cell Biology, Institute for Cancer Research, Oslo University Hospital, Montebello, 0379 Oslo, Norway

[#] These authors contributed equally

*Corresponding author. E-mail; anne.simonsen@medisin.uio.no

Keywords: mitophagy, autophagy, SNX10, endocytosis, mitochondria, mitochondrial homeostasis, ROS, zebrafish

Short title: SNX10 modulates mitochondrial homeostasis

eTOC summary:
Trachsel-Moncho et al. identify the endosomal protein SNX10 as a modulator of piecemeal mitophagy of OXPHOS machinery components and mitochondrial homeostasis. They show that loss of SNX10 enhances mitochondrial protein degradation, reduces respiration, and increases ROS levels leading to elevated cell death in vivo.

ABSTRACT

We here identify the endosomal protein SNX10 as a negative regulator of piecemeal mitophagy of OXPHOS machinery components. In control conditions, SNX10 localizes to early endocytic compartments in a PtdIns3P-dependent manner and modulates endosomal trafficking but also shows dynamic connections with mitochondria. Upon hypoxia-mimicking conditions, SNX10 localizes to late endosomal structures containing selected mitochondrial proteins, including COX-IV and SAMM50, and the autophagy proteins SQSTM1/p62 and LC3B. The turnover of COX-IV and the ATP synthase subunit pSu9 was enhanced in SNX10-depleted cells, with a corresponding reduced mitochondrial respiration and citrate synthase activity. Importantly, zebrafish larvae lacking Snx10 show reduced levels of COX-IV, as well as elevated ROS levels and ROS-mediated cell death in the brain, demonstrating the in vivo relevance of SNX10-mediated modulation of mitochondrial bioenergetics.

INTRODUCTION

Several diseases are characterized by an imbalance between protein production, sorting and degradation, making it important to understand the crosstalk between the pathways involved in regulation of proteostasis, including autophagy and endocytosis (Vagnozzi and Praticò 2019). While autophagy entails the sequestration of endogenous cytoplasmic material into double-membrane autophagosomes that fuse with lysosomes for cargo degradation (Y. Feng et al. 2014; Melia, Lystad, and Simonsen 2020), endocytosis generally involves lysosomal sorting of exogenous material. The autophagic and endocytic pathways are however closely connected, as autophagosomes can fuse with endocytic vesicles prior to their fusion with lysosomes and endosomes can contribute membrane to the growing autophagosome (Hyttinen et al. 2013). Moreover, components of the core autophagy machinery have been localized to endosomes, and components of the endosomal sorting complexes required for transport (ESCRT) are important for closure of the autophagosome (Rusten and Stenmark 2009). However, our knowledge about the molecular mechanisms involved in the regulation of the dynamic crosstalk between different types of autophagy and endocytosis remains sparse.

Mitophagy involves the selective degradation of mitochondrial material in lysosomes, preventing the accumulation of dysfunctional mitochondria to mitigate cellular stress. Dysregulation of mitophagy is linked to neurodegenerative diseases, metabolic disorders, and cancer, and it is therefore important to understand the mechanisms involved in mitophagy. Recently, it has been observed that early and late endosomes can interact with mitochondria (Das et al. 2016; Hamdi et al. 2016; Sheftel et al. 2007; Hammerling et al. 2017; Yamano et al. 2018; Prashar et al. 2024) and that such interactions may play a role in mitochondrial quality control and stress responses (Shutt and McBride 2013).

The PX domain-containing protein sorting nexin 10 (SNX10) was recently identified in a screen for lipid-binding proteins involved in Parkin-independent mitophagy (Munson et al. 2021). SNX10 is one of the simplest sorting nexin (SNX) proteins, consisting of a single PX domain that interacts with PtdIns(3)P (Chandra et al. 2019) and an intrinsically disordered region (IDR) in its C-terminal domain, as elucidated by AlphaFold (Jumper et al. 2021; Varadi et al. 2022). The IDR may account for the diverse cellular roles attributed to SNX10 and its implication in various pathologies (Holehouse and Kragelund 2023). SNX10 has been found to play a role in cilium biogenesis and promote the localization of vacuolar H^+-ATPase subunits and RAB8A to the cilium

(Chen et al. 2012). Moreover, several single nucleotide polymorphisms (SNPs) in SNX10 have been linked to autosomal recessive osteopetrosis (ARO) (Pangrazio et al. 2013; Amirfiroozy et al. 2017; Koçak et al. 2019; Stattin et al. 2017) a rare and heterogeneous genetic disease characterized by abnormally dense bone, where dysfunctional or absent osteoclasts fail at performing bone resorption (Pangrazio et al. 2013). Beyond ARO, SNX10 has emerged as a multifaceted player in various pathologies, including gastric cancer, glioblastoma, and colorectal cancer (Deng and Yuan 2024; Gimple et al. 2023; H. Feng et al. 2023). Moreover, SNX10 deficiency has been reported to reshape macrophage polarization towards an anti-inflammatory M2 phenotype (You et al. 2016), while its upregulation during bacterial infection enhances phagosome maturation and bacterial killing (Lou et al. 2017). Additionally, SNX10 expression seems to correlate with the severity of Crohn's Disease in both human and mouse models, suggesting its potential role in inflammatory bowel diseases (Bao et al. 2023). SNX10 has also been found to influence human adipocyte differentiation and function (Hansen et al. 2023). The involvement of SNX10 in diverse diseases, necessitates a deeper exploration of its molecular mechanisms and therapeutic potential.

Here, we show that SNX10 localizes to early and late endocytic compartments and that it modulates the turnover of selected mitochondrial proteins involved in respiration and ATP production, thereby preventing ROS production and cell death.

Results

SNX10 localizes to early and late endocytic compartments in a PtdIns3P dependent manner

To characterize the mechanisms underlying the normal function of SNX10 and its role in disease development, we generated U2OS cell lines with stable inducible expression of EGFP-tagged wild type (WT) SNX10 or SNX10 having mutations corresponding to ARO-linked SNPs (Y32S, R51P or R51Q), all located in the PX domain (Elson et al. 2021) of the canonical SNX10 isoform (Fig. 1 A, B and S1 A). We observed small cytosolic puncta and larger ring-shaped SNX10-positive structures in cells expressing WT SNX10-EGFP that were absent in cells expressing the ARO-linked mutants, all showing diffuse cytosolic localization (Fig. 1 C). The ARO mutant proteins seem more unstable, as several degradation products, not present in the WT cell lysate, were detected (Fig. 1 D).

The small SNX10-EGFP positive puncta colocalized extensively with early endosome antigen 1 (EEA1) and were often seen in very close proximity to larger SNX10-positive ring

structures, suggesting these might fuse (Fig. 1 E). The diffuse cytosolic staining of the SNX10 mutants (Fig. 1 C and E) indicates that the membrane localization of SNX10 is PtdIns3P dependent. Indeed, when treating cells with the PIK3C3 specific inhibitor VPS34-IN1, both the SNX10-EGFP positive puncta and the ring structures disappeared, as well as most of the EEA1 staining, as expected since EEA1 has a PtdIns3P-binding FYVE domain (Simonsen et al. 1998) (Fig. 1 E). The SNX10-positive vesicles were also positive for endogenous CD63 (a marker of late endosomes) (Fig. 1 F). Quantification revealed that SNX10-EGFP-positive structures colocalized to a similar extent with EEA1-positive and CD63-positive structures (Fig. 1 G). In line with a role for SNX10 at multiple stages of the endocytic pathway, SNX10-EGFP colocalized with mScarlet-RAB5 (Pankiv et al. 2024) (early endosomes), mScarlet-RAB7A (Pankiv et al. 2024) (a marker of early-to-late endosomes) and mScarlet-RAB9A (Pankiv et al. 2024) (involved in endosome-trans Golgi network trafficking) when stably expressed in SNX10-EGFP cells (Fig. S1 B). However, SNX10-EGFP did not colocalize with the recycling endosome markers mScarlet-RAB4 (Pankiv et al. 2024) and mScarlet-RAB11 (Pankiv et al. 2024), with mScarlet-RAB6 (Pankiv et al. 2024) (secretory pathway) or mScarlet-RAB43 (Pankiv et al. 2024) (retrograde transport) (Fig. S1 B).

As previously shown (Qin et al. 2006), expression of SNX10-EGFP led to the formation of giant juxtanuclear vacuoles (Fig. 1 C and Fig. S1 A). Remarkably, these big vacuoles were often negative for SNX10-EGFP and did not form in cells expressing mutant SNX10-EGFP (Y32S, R51P or R51Q) (Fig. 1 C and Fig. S1 A). The limiting membrane of the large vacuoles stained positive for CD63 (Fig. 1 F), LAMP1 (Fig. 1 H), and RAB7 (Fig. S1 B), and LysoTracker Red stained the vacuole lumen (Fig. S1 C), indicating an acidic lysosomal nature of the large SNX10-induced vacuoles.

To further characterize the nature of SNX10 positive vesicles, SNX10-EGFP cells were processed for correlative light and electron microscopy (CLEM) analysis (Fig. 1 I). When focusing on one of the SNX10-EGFP positive structures, we observed endocytic vesicles containing membranous material that were surrounded by an electron-dense environment of small vesicles (Fig. 1 I, iii-iv), where many appeared to be clathrin-coated vesicles (Fig. 1 I, iv-v, arrows). Indeed, using confocal imaging, we confirmed that SNX10-EGFP localizes with clathrin-positive structures (Fig. S1 D).

SNX10 promotes endocytic trafficking

The localization of SNX10 to both early and late endocytic compartments led us to investigate the potential role of SNX10 in endosomal trafficking. U2OS SNX10-EGFP cells were incubated with

an antibody against the epidermal growth factor (EGF) receptor (EGFR) on ice, followed by EGF-mediated stimulation of EGFR internalization (Fig. 2 A). As expected, SNX10-EGFP puncta showed a clear co-occurrence with endocytosed EGF and with EGFR after EGF stimulation (Fig. 2 B). To assess the potential role of SNX10 in EGFR trafficking, control and SNX10-depleted cells were incubated with EGF for 15 min to activate EGFR signaling and internalization, followed by a chase for up to 120 min. Intriguingly, the level of EGFR and the level of phosphorylated EGFR were higher in SNX10-depleted cells compared to control cells (Fig. 2, C and D), suggesting that SNX10 may affect early endocytic trafficking. In line with such a model, SNX10 silencing with two independent oligos significantly increased the numbers of EEA1-positive puncta (Fig. 2, E and F). Moreover, quantification of endosomes containing immunogold-labeled EGFR in sections from electron microscopy images revealed that EGFR-containing endosomes were significantly smaller in SNX10-depleted cells than in control cells (Fig. 2, G and H). Together, our data indicate a role for SNX10 in promoting early endocytic trafficking.

SNX10-positive endosomes contain mitochondrial material and colocalize with autophagy markers

To further understand the cellular function of SNX10, we set out to identify the interactome of SNX10 and compare it to the interactome of the ARO mutant SNX10 Y32S that does not bind to membranes. U2OS cells stably expressing SNX10-EGFP WT, SNX10-EGFP Y32S or EGFP (control), were subjected to GFP-trap pulldown experiments, followed by analysis of their respective interactome by mass spectrometry. A total of 53 proteins were identified as significant SNX10-EGFP interactors compared to the EGFP control, as analyzed by R lima using a cut-off value of log2FC > 1 and adjusted P-value < 0.05 (Fig. 3 A). Of these, 29 proteins were specific for WT SNX10 and 24 were common with the Y32S mutant (Fig. 3 A). GO term analysis showed that these 53 proteins included proteins with predicted localization (Cellular component) to endomembrane compartments (e.g., LAMTOR1, SQSTM1/p62, MVB12A), mitochondria (e.g., ATP5J, ATPIF1, COX-IV), endoplasmic reticulum (e.g., SERPINH1, TMEM109), and the extracellular space (e.g., YBX1, EEF1G). These proteins were associated with biological processes such as mitochondrial organization (e.g., COX-IV, UQCRFS1, SLC25A6), autophagy (e.g., LAMTOR1, GBA, SQSTM1), and endosome organization (e.g., SQSTM1, LAMTOR, MVB12A) (Fig. 3, A and B).

Given the interaction of SNX10 with mitochondrial (e.g., COX-IV, ATP5J, ATPIF1), autophagic (e.g., SQSTM1/p62) and endolysosomal (e.g., MVB12A, LAMTOR1) proteins (Fig. 3, A

and B), as well as its localization to early and late endosomes (Fig. 1 and Fig. S1), we speculated that SNX10 may have a function in the lysosomal turnover of mitochondrial material. To address this, U2OS SNX10-EGFP cells were labeled with MitoTracker Red and subjected to live cell imaging. SNX10-EGFP-positive structures were found to localize near the mitochondrial network and move along mitochondria in a highly dynamic manner, with occasional MitoTracker Red signal detected within SNX10 positive vesicles (Fig. 3 C and Movie 1). The SNX10 and MitoTracker Deep Red positive vesicles became noticeably bigger upon induction of mitophagy by the hypoxia-mimicking drugs DFP (deferiprone) (Fig. 3, D and E) or DMOG (dimethyloxalylglycine) (Fig. 4), both known to trigger mitophagy in a HIF1a-dependent manner(Allen et al. 2013). These vesicles also stained positive for mScarlet-RAB5 (Fig. 3 D) and the autophagy membrane protein LC3B (Fig. 3 E). The co-occurrence of LC3B-positive structures with SNX10 and with MitoTracker /SNX10-positive puncta were significantly increased in cells treated with DFP for 24 hrs (Fig. 3, F and G), indicating a functional shift in SNX10-positive structures upon induction of mitophagy. Indeed, while SNX10 vesicles largely colocalized with EEA1 under control conditions, with minimal co-localization with mitochondria or LC3B (Fig. 4, A and B), SNX10 vesicles showed reduced co-localization with EEA1, along with increased incorporation of mitochondria, LC3B and CD63 following DFP or DMOG treatment (Fig. 4, C and D). Taken together, our data indicate that SNX10 primarily localizes to early endosomes in control conditions and to mitochondria-containing LC3B and CD63 positive structures under hypoxia-mimicking conditions.

SNX10 modulates mitochondrial protein degradation

To decipher the nature of the mitochondrial cargo included in SNX10-positive vesicles, SNX10-EGFP cells were fixed and stained with antibodies against distinct mitochondrial proteins. Notably, the incorporation of ATP5J, SAMM50, and COX-IV into SNX10-EGFP vesicles was evident upon DFP treatment (Fig. 5 A), while TOMM20, TIMM23, and PDH were rarely detected (Fig. S2 A), although their mitochondrial staining was clear. SNX10 positive vesicles containing COX-IV also stained positive for endogenous LC3B (Fig. 5, B and C) and LAMP1 (Fig. 5, D and E) both in cells treated with DFP and DMOG (Fig. 5, B-E), suggesting a role for SNX10 positive vesicles in mitophagy.

To investigate whether SNX10 might regulate the turnover of mitochondrial proteins, we assessed the abundance of selected mitochondrial proteins in cells transfected with control or SNX10 siRNA that were treated or not with DFP for 24 hrs (Fig. 6 A). Interestingly, SNX10

depletion seems to reduce the abundance of several mitochondrial proteins, both at basal levels and upon mitophagy induction, with a significant effect on COX-IV levels (Fig. 6, A-D). Immunofluorescence staining for COX-IV also revealed a significant reduction of the staining intensity in cells depleted of SNX10, which was further reduced in DFP-treated cells (Fig. 6, E and F). In contrast, the level of the outer mitochondrial membrane (OMM) protein TOMM20 (Fig. S2, B and C) was unaffected by the depletion of SNX10. The reduced level of COX-IV seen in SNX10-depleted cells was not due to changes in COX-IV transcription (Fig. S2 D) or proteasomal degradation of COX-IV (Fig. S2 E), suggesting a role for SNX10 in the lysosomal clearance of selected mitochondrial proteins.

SNX10 is a negative modulator of piecemeal mitophagy

Given the co-localization of SNX10 with LC3B, we speculated that SNX10 may play a role in mitophagy. To address this, we used two different stable mitophagy reporter U2OS cell lines, one expressing the inner mitochondrial membrane (IMM) reporter, pSu9-Halo-mGFP (Wen-You Yim, Yamamoto, and Mizushima 2022), and one expressing the mitochondrial targeting signal of the matrix protein NIPSNAP1 tagged with EGFP-mCherry (referred to as iMLS) (Princely Abudu et al. 2019). The pSu9-Halo-mGFP cells allow a measure of mitophagy flux upon mitophagy induction with DFP or DMOG, as the cleaved Halo tag is stable in lysosomes when bound to the ligand (Fig. 7, A and B). The ratio of cleaved versus full-length pSu9-Halo-mGFP was analyzed by Western blotting (relative to a loading control), demonstrating a significant increase in mitophagy under both DFP and DMOG conditions in cells depleted of SNX10 compared to control cells (Fig. 7, A and C). In contrast, SNX10 depletion did not affect the lysosomal transport of the mCherry-EGFP-tagged matrix reporter, as analyzed by the area of red-only puncta (representing mitolysosomes due to quenching of the EGFP signal in acidic lysosomes) (Fig. S3, A and B). Thus, our data indicate a role for SNX10 as a negative regulator of lysosomal turnover of selected mitochondrial membrane components in response to HIF1 activation.

In addition to macro-mitophagy, other quality control pathways can facilitate the disposal of mitochondrial proteins for lysosomal degradation, including piecemeal mitophagy (Le Guerroué et al. 2017; Abudu et al. 2021), mitochondria-derived vesicles (MDVs) (Soubannier et al. 2012), and the VDIM (vesicles generated from the inner membrane) (Prashar et al. 2024) pathway. Besides colocalizing with LC3B, SNX10 vesicles containing mitochondrial material also were found to colocalize with p62 (Fig. 7, D), which argues against a role for SNX10 in the MDV

or VDIM pathways, as these are negative for LC3B and p62 and independent of the core autophagy machinery (Soubannier et al. 2012; Prashar et al. 2024). Indeed, the depletion of SNX10 neither affected the number of $PDH^{+}TOMM20^{-}$ nor $PDH^{-}TOMM20^{+}$ MDVs (Fig. S3, C and D).

Piecemeal mitophagy targets selected mitochondrial proteins to lysosomes, including components of the sorting and assembly machinery (SAM) complex and the mitochondrial contact site and cristae organizing system (MICOS) complex, and has been found to rely on p62 and the LC3 conjugation machinery proteins (Le Guerroué et al. 2017; Abudu et al. 2021). Indeed, COX-IV levels were significantly increased in p62-depleted cells (Fig. 7, E and F). Interestingly, neither the DFP-induced COX-IV clearance nor the reduced COX-IV levels seen in SNX10-depleted cells were recovered in cells treated with inhibitors of VPS34 (IN1 (Bago et al. 2014)) or ULK1 (MRT (Petherick et al. 2015)) (Fig. 7, G-I), both kinases being important for macroautophagy (Y. Feng et al. 2014), but yet unknown whether they are required for piecemeal mitophagy. In line with this, the DFP-induced co-occurrence of LC3B with SNX10 and SNX10/Mitotracker-positive structures was not affected in cells treated with the ULK1 inhibitor compared to control cells (Fig. 3, E-G). Taken together, our data indicate that SNX10 modulation of COX-IV turnover is independent of canonical macro-autophagy (Fig. 10).

SNX10 loss decreases mitochondrial bioenergetics

Given the interaction of SNX10 with ATP5J, a subunit of the mitochondrial ATP synthase (Fig. 3 A), and the increased degradation of pSu9-Halo-mGFP, another ATP synthase subunit (Fig. 7 A), and key electron transport chain proteins (COX-IV) (Fig. 6) in SNX10-depleted cells, we next investigated whether SNX10 depletion affects mitochondrial bioenergetics. Indeed, both the baseline OCR (oxygen consumption rate; an indicator of mitochondrial respiration) and the ATP-production linked respiration were decreased in U2OS cells lacking SNX10 compared to control cells, as analyzed by a Seahorse XF Analyzer (Fig. 8, A-C).

Interestingly, also the activity of citrate synthase (CS), an enzyme that catalyzes the first reaction of the Krebs cycle in the mitochondrial matrix, was decreased in SNX10-depleted cells compared to control cells, both under basal conditions and upon treatment with DFP for 24 hrs (Fig. 8 D). The level of CS is often used as a read-out for the total mitochondrial level (Shepherd and Garland 1969). However, the reduction in CS activity did not correlate with reduced CS levels as determined by Western blotting (Fig. 8, E and F), suggesting a lower activity of the Krebs cycle

and further demonstrating the selectivity of SNX10 in the degradation of mitochondrial proteins. Taken together, our data indicate that SNX10 is important for normal mitochondrial bioenergetics.

Snx10 is partially conserved in zebrafish and expressed during early embryogenesis

To validate the potential role of SNX10 in piecemeal mitophagy *in vivo*, we employed zebrafish as a model system. Zebrafish contain SNX10 paralogues (s*nx10a* and *snx10b)* that are ~60% similar to one another and ~59% homologous to human SNX10 with the N-terminal PX domain being the most highly conserved (~71% and ~63.5%, respectively) (Fig. 9 A). We first sought to examine the spatiotemporal expression pattern of *snx10a* and *snx10b* during the early development of zebrafish. While both *snx10a* and *snx10b* were consistently expressed from 1 day post fertilization (dpf) to 5 dpf as determined by real-time qPCR, *snx10a* transcripts were more abundant than *snx10b* transcripts (Fig. 9 B), suggesting the importance of *snx10a* in the early development of the zebrafish larvae. Whole-mount in situ hybridization (WM-ISH) of *snx10a* and *snx10b* transcripts in 2 dpf to 5 dpf wild-type zebrafish larvae revealed expression of *snx10a* in the retina, optical tectum, intestine, midbrain, and hindbrain at all time points, whereas *snx10b* transcripts were found mainly in the retina and notochord at 2-5 dpf, and in the whole brain at 5 dpf (Fig. 9 C and Fig. S4 A). There was no staining of the control sense probe at any time points.

Increased turnover of mitochondrial proteins in zebrafish larvae lacking Snx10

To explore a possible role for Snx10-regulated mitophagy in the early development of zebrafish larvae, we employed CRISPR/Cas9-mediated genome editing in zebrafish embryos using guide sequences targeting *snx10a* and *snx10b* individually or together (*snx10ab* double knockout (DKO)) (Fig. S4 B). The loss of Snx10 protein in DKO larvae compared to larvae injected with control oligo was verified via immunoblotting (Fig. 9 D)

Control and *snx10ab* DKO larvae were treated or not with 100 µm DMOG for 24 hrs at 2 dpf to induce mitophagy (Munson et al. 2021), as demonstrated by a significant upregulation of *bnip3* mRNA levels (Fig. S4 C). In line with our data obtained in SNX10-depleted U2OS cells, the Cox-IV protein level was significantly reduced in *snx10ab* DKO larvae when compared to controls (Fig. 9, E and F). Samm50 was also reduced in *snx10ab* DKO larvae at the basal level and upon DMOG treatment (Fig. 9, E-G), but neither *cox-IV* nor *samm50* mRNA levels were significantly

reduced (Fig. S4 D), indicating a role for snx10 in the turnover of zebrafish Cox-IV and Samm50 proteins.

Snx10 affects cell death and oxidative stress in zebrafish

Most *snx10ab* DKO larvae showed a dysmorphic phenotype (data not shown) with necrotic tissue damage in the head and trunk region, suggesting possible cell death. To further investigate this, we performed TUNEL (terminal deoxynucleotidyl transferase dUTP nick end labeling) staining on sections of fixed control and *snx10ab* DKO larvae, treated with or without DMOG, followed by confocal microscopy and quantification of the mean fluorescent intensity in the brain (region of interest, ROI, indicated) (Fig. 9, H and I), having high *snx10* expression (Fig. 9 C). TUNEL staining showed increased cell death in *snx10ab* DKO larvae relative to control (Fig. 9, H and I). Interestingly, DMOG-treated control larvae also showed increased cell death as compared to control larvae (Fig. 9, H and I), which may suggest that increased turnover of mitochondria, caused by snx10 depletion or DMOG treatment, promotes cell death. To assess whether the increased cell death seen in *snx10ab* DKO larvae could be attributed to increased oxidative stress, control and *snx10ab* DKO zebrafish larvae were trypsinized and treated with deep red MITOSOX dye before FACS analysis. Indeed, there was a significant increase in ROS levels in *snx10ab* DKO larval cells as compared to the control (Fig. 9 J and Fig. S4 E). Importantly, the increased TUNEL staining seen in *snx10ab* DKO larvae could be rescued with the addition of the antioxidant N-acetyl cysteine (NAC) (Fig. 9, K and L). Taken together, our *in vivo* data show an important role for snx10 in preventing cell death and oxidative stress.

Discussion

In this manuscript, we identify the small PX domain protein SNX10 as a novel modulator of piecemeal mitophagy and mitochondrial bioenergetics. SNX10 localizes to early and late endocytic compartments in a PtdIns3P-dependent manner and modulates trafficking in the endosomal pathway. Upon hypoxia, SNX10 localizes to CD63-positive late endosomes containing mitochondrial material and autophagy proteins. We demonstrate that SNX10 functions as a negative regulator of piecemeal mitophagy of OXPHOS machinery components (including COX-IV and ATP synthase subunits) in response to hypoxia, allowing the cell to regulate oxidative phosphorylation in response to metabolic needs without compromising overall mitochondrial

structure. Zebrafish larvae lacking Snx10 are characterized by increased ROS and ROS-induced cell death, demonstrating an important role for Snx10 *in vivo*.

Mutations in SNX10 are linked to autosomal recessive osteopetrosis (ARO) (Pangrazio et al. 2013; Amirfiroozy et al. 2017; Koçak et al. 2019; Stattin et al. 2017), a life-threatening rare type of skeletal dysplasia characterized by increased bone density. All described ARO-linked mutations in SNX10 are found in the PX domain (Amirfiroozy et al. 2017; Koçak et al. 2019; Stattin et al. 2017), and we here show that three such mutants (Y32S, R51P and R51Q) fail to localize to endocytic compartments. The exact endosomal function of SNX10 is unclear, but the presence of enlarged LAMP1-positive vacuoles in cells expressing wild-type SNX10, but not ARO mutants, suggests that SNX10 may regulate fission/fusion events in the endocytic pathway. This is in line with previous data showing that mutation of the predicted Ptdns3P binding residue of SNX10 (Arg/R^{53}) prevents the formation of large vacuoles (Qin et al. 2006), suggesting that PtdIns3P-mediated endosome recruitment of SNX10 is important for its normal function and prevention of ARO. SNX10 is the smallest of the PX domain proteins, containing only a PX domain plus a short IDR (intrinsically disordered region), generally known for their dynamic and adaptable nature, existing in a repertoire of structurally distinct conformations that rapidly interconvert based on their cellular context (Holehouse and Kragelund 2023). SNX10 pulldown experiments demonstrated that the ARO mutant (Y23S) interacted with more proteins than the WT SNX10, so it is also possible that SNX10 PX mutants may cause ARO through its C-terminal IDR.

Mitochondria are crucial for the regulation of nutrient metabolism and maintenance of bone homeostasis. Currently, a potential association between ARO and mitochondrial dysfunction is not known. However, mitochondrial dysfunction, including impaired mitochondrial autophagy and OXPHOS activity, as well as ROS accumulation, has been linked to osteoporosis (Liu, Gao, and Liu 2024).

We found that SNX10 interacts with proteins belonging to the mitochondrial cell compartment and that depletion of SNX10 promotes the degradation of selected mitochondrial proteins, including the inner mitochondrial membrane (IMM) proteins COX-IV and an ATP synthase subunit (pSu9-Halo-EGFP), with no effect on a mCherry-EGFP-tagged matrix marker or the total mitochondrial abundance. Cells lacking SNX10 also had decreased OXPHOS activity. These results are in line with previous reports showing increased glucose metabolism upon SNX10 depletion in intestinal epithelial cells (H. Feng et al. 2023) and increased levels of LAMP2A (You et al. 2018; Lee et al. 2022).

Our data indicate that SNX10 functions as a negative modulator of piecemeal mitophagy of COX-IV. Using hypoxia-mimicking drugs (DFP and DMOG), we observed staining of COX-IV within SNX10-positive vesicles that co-localized with markers of late endosomes (CD63) and lysosomes (LAMP1), as well as the autophagy proteins LC3B and p62/SQSTM1. Intriguingly, neither the DFP- nor the siSNX10-induced degradation of COX-IV or the co-localization of SNX10 with LC3B was reduced by inhibition of the core autophagy machinery components ULK1 or VPS34, suggesting a non-canonical type of mitophagy. It is not known whether piecemeal mitophagy depends on ULK1 or VPS34, but it has been shown to rely on p62/SQSTM1 (Le Guerroué et al. 2017; Abudu et al. 2021). Indeed, we show that p62 co-localizes with COX-IV and that depletion of p62 leads to increased COX-IV levels. The seemingly selective effect of SNX10 on the turnover of proteins involved in mitochondrial oxidative phosphorylation and ATP production is reminiscent of the recently described VDIM (Vesicles Derived from the Inner Mitochondrial membrane) pathway (Prashar et al. 2024). VDIMs are formed by IMM herniation through pores in the outer mitochondrial membrane, followed by their engulfment by lysosomes in proximity to mitochondria in a microautophagy-like process. VDIM formation was found to increase upon oxidative stress, leading to selective degradation of IMM proteins (including COX4 and other proteins involved in OXPHOS) while sparing the remainder of the organelle. However, in contrast to the observed MitoTracker/COX-IV-containing SNX10-positive vesicles, VDIMs seem to lack LC3 and p62. We also show that mitochondria-derived vesicles form independently of SNX10. Thus, we conclude that SNX10 functions as a negative modulator of piecemeal mitophagy of Cox-IV upon hypoxia. We speculate that the SNX10 interactome may change in response to various metabolic conditions, thereby modulating the lysosomal transport of endocytic and mitochondrial cargo to allow the cell to respond to the metabolic needs of the cells.

Importantly, the depletion of Snx10 in zebrafish larvae also caused a reduction of Cox-IV and Samm50 protein levels, with a corresponding increase in reactive oxygen species (ROS), indicating a conserved role of Snx10 *in vivo* as a modulator of mitochondrial homeostasis. Elevation of cell death in *snx10ab*-depleted fish could be attributed to ROS-mediated cell death as it was rescued by antioxidant treatment. While decreased levels of mitophagy previously have been linked to increased ROS and cell death (Baechler, Bloemberg, and Quadrilatero 2019; Lin et al. 2019), our data indicate that also increased turnover of selected mitochondrial proteins can cause ROS and cell death in vivo. In line with such a model, induction of mitophagy using the hypoxia mimetic drug DMOG in control larvae significantly increased cell death, suggesting that

excess mitophagy may trigger cell death (Ma, Han, and Zhan 2024). Dynamic interactions between mitochondria and endolysosomes have also been linked to pathogen killing by the transfer of mitochondrial ROS to phagosomes containing bacteria (Abuaita, Schultz, and O'Riordan 2018). It is interesting to note that SNX10 has been related to pathologies connected to monocyte/macrophage malfunctioning (You et al. 2016; Lou et al. 2017).

In conclusion, we here present data showing that SNX10 modulates piecemeal mitophagy of selective OXPHOS machinery proteins under hypoxia-mimicking conditions, allowing cells to dispose of surplus mitochondrial components without affecting the larger mitochondrial structures. Lack of SNX10 leads to an accumulation of ROS and ROS-induced cell death, uncovering a previously unknown role of SNX10 in mitochondrial homeostasis. This unexpected association opens avenues for further exploring the intricate interplay between endocytic and mitochondrial pathways, emphasizing SNX10's crucial role in cellular homeostasis and providing a foundation for future investigations in both physiological and pathological contexts.

Materials and Methods

Antibodies and dyes

Primary antibodies used: Anti-HaloTag (Promega, G9211, 1:1000, ms), ATP5J (Atlas Antibodies, HPA031069, 1:200, rb), β-Actin (Cell Signaling Technology, #3700, 1:5000, ms), CD63 (DHB, #H5C6, 1:200, ms) Citrate Synthase (Cell Signaling Technology, #14309, 1:1000, rb), Clathrin (Acris, #SM5011P, 1:200), COX-IV (Cell Signaling Technology, #4850S, 1:1000 for WB and 1:200 for IF, rb), EEA1 (BD Biosciences, #610457; 1:250, ms), GAPDH (Abcam, Ab9484, 1:5000, ms), GAPDH (Cell signaling, #5174, 1:1000, rb), GFP (Takara, # 632569, 1:1000, ms) EGFR (Fitzgerald, #20-ES04, 1:1000 for WB and 1:200 for IF, sh), P-EGFR (Tyr1068) (Cell Signaling, #3777, 1:1000, rb), PDH (Cell Signaling Technology, #2784S, 1:1000 for WB and 1:200 for IF, rb), LAMP1 (Santa Cruz Biotechnology, #sc-20011, 1:250, ms), LC3B (MBL, #PM036, 1:250, rb), SAMM50 (Novus Biologicals, NBP1-84509, 1:200, rb), SNX10 (Atlas Antibodies, HPA015605, 1:1000, rb), alpha Tubulin (GeneTex, GTX628802, 1:5000, ms), TIMM23 (BD Biosciences, # 611223, 1:1000 for WB 1:250 for IF, ms), TOMM20 (Santa Cruz, #17764, 1:200, ms).

Secondary antibodies used for immunoblotting: DyLight800 mouse and rabbit (Invitrogen, #SA5-10172 and #SA5-10044), StarBright Blue 700 mouse and rabbit (Bio-Rad, #12004158 and

#12004161), Peroxidase AffiniPure™ Goat Anti-Mouse IgG (H+L) (Jackson, #115035003, #1:5000), Peroxidase AffiniPure™ Goat Anti-Rabbit IgG (H+L) (Jackson, #111035144, 1:5000). Fluorescent dyes used include: MitoTracker™ Deep Red FM (ThermoFisher, #M22425), MitoTracker™ Red CMXRos (ThermoFisher Scientific, #M7512), LysoTracker™ Red DND-99 (ThermoFisher # L7528), Hoechst 33342 (Invitrogen, #H1399).

Cell culture and reagents

U2OS TRex FlpIn cells (kindly provided by Steve Blacklow, Harvard Medical School, US) were used for generation of stable inducible cell lines. They were maintained in a complete medium of Dulbecco's Modified Eagle Medium (DMEM – Lonza 12-741F) supplemented with 10% fetal bovine serum (FBS – Sigma Aldrich #F7524), 100 U/ml penicillin and 100 µg/ml streptomycin (ThermoFisher Scientific #15140122). Cells were kept in a humidified incubator at 37 °C and 5% CO_2. For starvation conditions, the cells were incubated 2-4 hrs in Earle's balanced salt solution (EBSS; Gibco, # 24010043). Bafilomycin A1 (referred as BafA1, BML, #CM110) was used at 100 nM. Deferiprone (DFP; Sigma Aldrich, #379409) was used at 1 mM. Doxycycline (Clontech, #631311) was used at 100 ng/ml. EGF VPS34-IN1 (Selleckchem, # S7980) was used at 5 µM. Tetramethylrhodamine (TMR)-conjugated ligand (Promega, G8251) was used at 100 nM for 20 min.

Cell transfection

For the generation of stable cell lines U2OS FlpIn TRex cells were transfected with pcDNA5/FRT/TO-SNX10-EGFP wild type or mutant constructs (Table 1) using Lipofectamine 2000 (Invitrogen, #11668019). Positively transfected cells were selected with hygromycin B (EMD Millipore, #400052). Doxycycline was used at 100 ng/ml for 24 hrs to induce protein expression. Cell lines expressing mScarlet-tagged RAB proteins were created with lentiviral transduction. Briefly, 293FT cells were co-transfected with psPAX2 and pCMV-VSVG plasmids to generate lentiviral particles. These particles were transduced, after harvesting and filtering, into the SNX10-EGFP stable cell line together with 10 ug/ml polybrene (Santa Cruz, sc-134220) and selected using puromycin (Sigma #P7255). The plasmids used for the cell lines creation are compiled in Table 1. Point mutations were introduced by using the QuickChange site-directed mutagenesis kit (Agilent Technologies) and the primers used for this are listed in Table 1.

For siRNA transfections, cells were incubated with Silencer Select siRNA oligonucleotides targeting each gene at 20 nM, in combination with RNAiMAX (Invitrogen, #13778150) through reverse transfection. The cells were fixed/harvested for further procedures after 72 hrs of knockdown.

Citrate Synthase Assay

Biochemical quantification of mitochondrial abundance was done by analysis of citrate synthase activity. Briefly, U20S cells were plated and grown as described in the figure legend. The cells were harvested after washing twice with PBS on ice and then lysed in NP-40 lysis buffer (50 mM HEPES pH 7.4, 150 mM NaCl, 1 mM EDTA, 10% (v/v) NP-40 + 1 mM DTT, it also contained 1x Phosphatase inhibitors and 1x Protease inhibitors added fresh). Cell lysates were centrifuged at 21000 x g for 10 min at 4°C and the supernatant was obtained. The protein concentration was quantified by Bradford assay. To determine the citrate synthase activity, 0.4 µl of cell lysate was added to 198 µl of CS assay buffer (100 mM Tris pH 8, 0.1% Triton X-100, 0.2 mM DTNB (5,5'Dithiobis (2-nitrobenzoic acid)), 0,1mM Acetyl CoA). At the starting point, 2µl of 20 mM Oxaloacetate was added and the plate was incubated at 35°C. The reactions were monitored in a FLUOstar OPTIMA plate reader (BMG Labtech) at λ_{Abs}= 440 nm. The reactions were scanned each 87s for a total of 40 cycles. The values were compared to the Oxaloacetate lacking controls. The rate of the reactions was plotted to determine the citrate synthase activity and the activity rate was calculated using the linear part of the curve, before saturation was reached. Then the values were normalized to protein concentration and then normalized to control value. The graph displays relative values.

Immunofluorescence

The cells were seeded onto glass coverslips or 96 well plates for high-throughput imaging. siRNA treatment lasted for 72 hrs and stable cell lines were subjected to doxycycline for 24 hrs prior to treatments to allow protein expression, as indicated in figure legends. After treatments, the cells were washed with PBS and then fixed with PFA fixation buffer (3.7% (w/v) PFA, 200mM HEPES pH 7.0) for 20 min. After fixing, the cells were washed twice with PBS and then permeabilised for 5 min with 0.2% (v/v) NP-40 in PBS. Cells were then washed once and then incubated for blocking for 15 min with 1% BSA in PBS solution (IF blocking solution). After blocking, the coverslips were incubated with the primary antibodies for 1 hr at 37 °C (antibodies were diluted in IF blocking

solution at the dilutions stated in the section “Antibodies and dyes”) and then washed 3x10 min in IF blocking solution. After washing the cells were incubated with their corresponding secondary antibodies again diluted in IF blocking solution at the concentrations above stated, for 30 min at room temperature (RT). Finally, the cells were washed again with IF blocking solution and then incubated with Hoechst 33342 diluted in 1xPBS at 1µg/ml for 30 min. Coverslips were mounted in ProLong Diamond Antifade Mountant (Invitrogen, #p36965).

Live-cell imaging, high content immunofluorescence microscopy and confocal microscopy.

Imaging settings (laser intensity, time exposure, number of sections per z-stack and the stepsize between them, time intervals during live imaging) were set identically within each experiment to allow an optimal and non-saturated fluorescent imaging. For widefield imaging we used an ImageXpress Micro Confocal microscope from Molecular devices at 20x magnification. Live imaging and imaging of fixed cells were acquired using a Dragonfly 505 spinning disk confocal microscope (Andor Technology) utilizing a 63x or 100x oil objective (1.45 NA) and Zyla 4.2 sCMOS 2,048 x 2,048 camera. The spinning disc confocal mode was used for all pictures. The microscope was equipped with an Okolab cell incubator with temperature, CO_2 and humidity control for live cell imaging. Fixed cells were imaged at room temperature. If any other microscope was used, it will be specified in the figure legend.

EGF treatment

U2OS FlpIn TRex pcDNA5-SNX10-EGFP cells transfected with control or SNX10 siRNA for 72 hrs were then serum starved for 2 hrs in media supplemented with 10 µg/ml Cycloheximide, followed by addition of 50 ng/ml EGF (Santa Cruz Biotechnology, sc-4552) in combination with 10 µg/ml Cycloheximide (Sigma, C7698) for 0, 15, 30, 60and 1200 min. The cells were either fixed after 15 min for immunofluorescence or harvested at aforementioned time points and lysed as described on the Western Blotting section.

Image analysis

The identification of relevant structures was carried out using CellProfiler software (v4.2) (Stirling et al. 2021). The images were separated into individual channels and enhanced to improve the visibility of key features. Nuclei, cells, and puncta were detected by applying a manual threshold to segment the areas of interest, allowing for the calculation of puncta counts

per cell. Co-localization was assessed by relating the structures of interest and applying a mask that defined regions based on previously identified objects in the analysis pipeline. The percentage of co-localization was calculated using the measurements generated by these modules. In the IMLS cell analysis for mitophagy, mCherry-only structures were distinguished by calculating the ratio of the mCherry signal to the EGFP signal on a per-pixel basis, following background noise reduction. The intensity of the red signal was adjusted to correspond with the green signal in controls treated with Bafilomycin A1. The intensity was measured by using the "MeasureObjectIntensity" module and by taking into consideration "Integrated intensity" as a final measurement that represents the sum of pixel intensities within each object. This data was plotted as z-score, in which the values for each field of view were normalized by subtracting the mean and dividing by the standard deviation of the control group.

Oxygen consumption rate measurement

SNX10 was depleted as described above for a total of 72 hrs. Prior starting the experiment, the cells were resuspended in complete DMEM and seeded into Seahorse XFe24 Cell Culture microplates where they reached confluency. The plate was incubated at 37 °C in a humidified incubator. The media was then replaced with DMEM without Sodium Bicarbonate (pH 7.4) before analysis with the Seahorse XFe24 Analyzer (XF mito stress test, Agilent). Specific mitochondrial inhibitors were dissolved in DMEM and loaded into the injector ports of the Seahorse Sensor Plates. The final concentrations of the mitochondrial inhibitors were: CCCP: 1 µM, Oligomycin: 1.5 µM, Rotenone: 0.5 µM, Antimycin A: 0.5 µM. After the analysis, the cells were washed in ice cold PBS and lysed with NP-40 lysis buffer for protein quantification using BCA Assay (Thermo Fisher). Quantification was performed using the Seahorse Analytics software (seahorseanalytics.agilent.com, Agilent), with normalization based on the measured protein concentration from each well.

RNA Isolation, cDNA synthesis and qPCR

For quantifying the knockdown efficiency throughout the different experiments, RNA was isolated using the RNeasy Plus Mini Kit (Qiagen), except for RNA from experiments containing DFP, that was isolated using Trizol (ThermoFisher Scientific, #15596026). cDNA was synthesized using Superscript III reverse transcriptase (ThermoFisher Scientific, #18080085) and amplified using KAPA SYBR FAST qPCR Kit and designed primers targeting specific genes. For experiments

performed in a 96 well format the Power SYBR Green Cells-to-CT kit (ThermoFisher Scientific, #4402955) was used for extraction and amplification according to manufacturer's instructions. All amplification experiments were run in a CFx96 real-time PCR system (Bio-Rad). Transcript levels were normalized to TATA-box-binding protein (TBP) and the quantifications were performed using the $2^{-\Delta\Delta Ct}$ method. The primers used for real time PCR in this study are BNIP3: 5'GGCCATCGGATTGGGGATCT3' (fwd) and 5'GGCCACCCCAGGATCTAACA3' (rev). BNIP3L: 5'TCCACCCAAGGAGTTCCACT3' (fwd) and 5'GTGTGCTCAGTCGCTTTCCA3' (rev). COX-IV: 5'CAGTGGCGGCAGAATGTTG3' (fwd) and 5'GATAACGAGCGCGGTGAAAC3' (rev). HI1a: 5'GGCAGCAACGACACAGAAAC3' (fwd) and 5'GCAGGGTCAGCACTACTTCG3' (rev). SNX10: 5'TTGAGGCGTGTGTTTCTGGG3' (fwd), and 5'CCAAGCCCAGAGGATGAACTTT3' (rev). TBP: 5'CAGAAAGTTCATCCTCTGGGCT3' (fwd), and 5'TATATTCGGCGTTTCGGGCA3' (rev). TIMM23: 5' GATACCATGGAAGGAGGCGG3' (fwd) and 5'ATCCCTCGAAGACCACCTGT3' (rev). TOMM20: 5'GCTGGGCTTTCCAAGTTACC3' (fwd) and 5'AGTAACTGCTGTGGCTGTCC3' (rev). 'ULK1: 5'GTTCCAAACACCTCGGTCCT3' (fwd), and 5'TCCACCCAGAGACATCTTCCT3'.

RNA isolation from zebrafish larvae were performed using Trizol reagent (ThermoFisher Scientific, #15596026). cDNA was synthesized using Superscript III reverse transcriptase (ThermoFisher Scientific, #18080085), and amplified using KAPA SYBR FAST qPCR Kit. Primers targeting specific genes were designed. Transcript levels were normalized to beta-actin and the quantifications were performed using the 2-ΔΔCt method. Primers used for real-time PCR for zebrafish are: snx10a – 5'AGCTATGAGATCTGCCTTCACACC3' (fwd), and 5'TGACGCAGCCAAACAAACTCAC3' (rev); snx10b – 5'AGATTTCTGGCATGCCTTCATGG3' (fwd), and 5'AGTGAACGCCAAGCTGTTTGTATG3' (rev); cox-iv – 5'CTGCCTTCGTGGTGCACATG3' (fwd), and 5'GTCCTCGACCTTCGCAACT3' (rev); samm50 – 5'GGAACAACGAGGGCAGCATG3' (fwd), and 5'GGCAGTTTGATCCCCAGGAC3' (rev); bnip3l – 5'AGCAGCTCGTCCTGCAACAG3' (fwd), and 5'GGACTGTGTGGCCGTGGAGG3' (rev). bnip3 and beta-actin primers were from Qiagen (QT02053933 and QT02174907 respectively).

Correlative light and electron microscopy

For CLEM, U2OS FlpIn cells, stably expressing SNX10-EGFP were seeded on photo-etched coverslips (Electron Microscopy Sciences, Hatfield, USA). Cells were fixed in 4% formaldehyde, 0.1% glutaraldehyde in 0.1 M PHEM (240 mM PIPES, 100 mM HEPES, 8 mM MgCl2, 40 mM EGTA), pH 6.9, for 1 hr. The coverslips were washed with 0.1M PHEM buffer and mounted with Mowiol

containing 1µg/ml Hoechst 33342. The cells were examined with a Dragonfly 505 spinning disk confocal microscope (Andor Technology) using an oil immersed 60x magnification objective. Cells of interest were identified by fluorescence microscopy and a Z-stack covering the whole cell volume was acquired. The relative positioning of the cells on the photo-etched coverslips was determined by taking a low magnification DIC image. The coverslips were removed from the object glass, washed with 0.1 M PHEM buffer and fixed in 2% glutaraldehyde/0.1 M PHEM overnight. Cells were postfixed in osmium tetroxide and potassium ferry cyanide, stained with tannic acid, and uranyl acetate and thereafter dehydrated stepwise to 100% ethanol followed by flat-embedding in Epon. Serial sections (200nm) were cut on a Ultracut UCT ultramicrotome (Leica, Germany) and collected on formvar coated slot-grids.

Sections were observed at 200 kV in a Thermo ScientificTM TalosTM F200C microscope and recorded with a Ceta 16M camera. For tomograms, image series were taken between -60° and 60° tilt angles with 2° increment. Single-axes tilt series were recorded with a Ceta 16M camera. Tomograms were computed using weighted back projection using the IMOD package. Display, segmentation and animation of tomograms were also performed using IMOD software version 4.9(Kremer, Mastronarde, and McIntosh 1996).

To assess the diameter of endosomes, U2OS cells subjected to SNX10 silencing were grown on poly-l-lysine coated sapphire discs. To label newly internalized EGFR following EGF-stimulation, cells were first washed in ice cold PBS and incubated with an antibody recognizing the extracellular part of EGFR (mouse anti-EGFR, Pharmingen) on ice. After washing four times with ice cold PBS, cells were incubated with Protein A-10 nm gold conjugate (UMC Utrecht Dept. of Cell Biology) which recognizes the Fc region of the mouse IgG2b primary antibody. Cells were again washed four times with ice cold PBS, stimulated with EGF in warm DMEM for 40 min and finally high pressure frozen using a Leica HPM100. Freeze substitution was performed as follows: sample carriers designed for sapphire discs were filled with 4 ml of freeze substituent (0.1% (w/v) uranyl acetate in acetone, 1% H2O) and placed in a temperature-controlling AFS2 (Leica) equipped with an FPS robot. Freeze-substitution occurred at -90 °C for 48 hrs before the temperature was raised to -45°C over a time span of 9 hrs. The samples were kept in the freeze substituent at -45 °C for 5 hrs before washing 3 times with acetone followed by a temperature increase (5 °C per hour) to -35 °C. Samples were stepwise infiltrated with increasing concentrations of Lowicryl HM20 (10%, 25%, 75%, 4 hrs each). During the last two steps, the temperature was gradually raised to -25°C before infiltrating 3 times with 100% Lowicryl (10 hrs

each). Subsequent UV-polymerization was initiated for 48 hrs at -25 °C, and the temperature was then evenly raised to +20 °C (5 °C per hour). Polymerization then continued for another 24 hrs at 20 °C. Serial sections (250 nm) were cut on an Ultracut UCT ultramicrotome (Leica, Germany) and collected on formvar coated slot grids.

Single-axis tilt tomograms were collected in a Thermo ScientificTM TalosTM F200C microscope equipped with a with a Ceta 16M camera and image series were taken between -60° and 60° tilt angles with 2° increment. Tomograms were reconstructed using weighted back projection using the IMOD package software version 4(Kremer, Mastronarde, and McIntosh 1996).

SNX10 pull-down for interactome analysis

To analyse the SNX10-EGFP interactome, we used mass spectrometry assays in biological triplicates. U2OS cells expressing SNX10-EGFP, SNX10(Y32S)-EGFP or EGFP were lysed with NP-40 lysis (50 mM HEPES pH 7.4, 150 mM NaCl, 1 mM EDTA, 10% Glycerol, 0.5% NP-40) supplemented with PhosStop phosphatase inhibitor (Sigma) and cOmplete protease inhibitor cocktail (Merck). The protein purification was performed using ChromoTek GFP-Trap®, following the vendor's specifications. The mass spectrometry experiments were performed at the Proteomics Core Facility at Oslo University Hospital (Rikshospitalet). Beads were washed twice with 50 mM ammonium bicarbonate. Proteins on beads were reduced and alkylated and further digested by trypsin for overnight at 37°C. Digested peptides were transferred to new tube, acidified and the peptides were de-salted for MS analysis.

LC-MS/MS

Peptides samples were dissolved in 10 µl 0.1% formic buffer and 3 µl loaded for MS analysis. LC-MS/MS analysis of the resulting peptides was performed using an Easy nLC1000 liquid chromatography system (Thermo Electron, Bremen, Germany) coupled to a QExactive HF Hybrid Quadrupole-Orbitrap mass spectrometer (Thermo Electron) with a nanoelectrospray ion source (EasySpray, Thermo Electron). The LC separation of peptides was performed using an EasySpray C18 analytical column (2 µm particle size, 100 Å, 75 µm inner diameter and 25 cm; Thermo Fisher Scientific). Peptides were separated over a 60 mins gradient from 2% to 30% (v/v) ACN in 0.1% (v/v) FA, after which the column was washed using 90% (v/v) ACN in 0.1% (v/v) FA for 20 min (flow rate 0.3 µL/min). All LC-MS/MS analyses were operated in data-dependent mode where

the most intense peptides were automatically selected for fragmentation by high-energy collision-induced dissociation.

Raw files from LC-MS/MS analyses were submitted to MaxQuant 1.6.17.0 software(Cox and Mann 2008) for peptide/protein identification. Parameters were set as follow: Carbamidomethyl (C) was set as a fixed modification and PTY; protein N-acetylation and methionine oxidation as variable modifications. First search error window of 20 ppm and mains search error of 6 ppm. Trypsin without proline restriction enzyme option was used, with two allowed miscleavages. Minimal unique peptides were set to one, and FDR allowed was 0.01 (1%) for peptide and protein identification. The Uniprot human database was used. The generation of reversed sequences was selected to assign FDR rates.

The analysis of label-free intensities was performed with Perseus (Tyanova et al. 2016). The proteins with contaminants were omitted from the analysis. We used R (R Core Team, 2020) (Team 2020) limma (Ritchie et al. 2015) for performing imputation of missing values, fold change analysis and pValues were adjusted using the default adjust method used by topTable() command of limma R package. Gene ontology (GO) enrichment analysis for biological processes and cellular component was performed using DAVID (Database for Annotation, Visualization, and Integrated Discovery) with false discovery rate (FDR) correction to identify significantly enriched terms. Piecharts and Venn diagrams were plotted using ggplot2 R package and InteractiVenn (Heberle et al. 2015), respectively. The mass spectrometry proteomics data have been deposited to the ProteomeXchange Consortium via the PRIDE (Perez-Riverol et al. 2022) partner repository with the dataset identifier PXD056720.

Western blotting

For western blotting, the cells were treated as indicated in each experiment and then moved onto ice prior lysing. Briefly, the cells were washed twice with PBS and then lysed on ice in NP-40 lysis buffer (50mM HEPES pH 7.4, 150mM NaCl, 1mM EDTA, 10% Glycerol, 0.5% NP-40) supplemented with protease and phosphatase inhibitors (unless specified otherwise). The cells were incubated for 10 min and then collected. The samples were then centrifuged at 21000xg at 4°C during 10 min and then the supernatant was collected. Protein quantitation was assessed by Bradford assay (Bio-Rad #5000006) using serial dilutions of bovine serum albumin (BSA) as standards. Samples were then normalized and added to sample buffer (2.8x NuPage LDS Sample buffer + DTT 0.30M). After running the samples by an SDS polyacrylamide gradient gel (4–20%

Criterion™ TGX™ Precast Midi Protein Gel, Bio-Rad) and transferring them to a PVDF membrane (350mA/1h), the samples were blocked with casein buffer (0.5% Casein, 0.1%, NaAzide, PBS) for 1h at RT and then incubated overnight at 4°C with primary antibodies. Primary antibodies were diluted in a 5% BSA in PBST solution (1X Phosphate-Buffered Saline, 0.1% Tween® 20 Detergent). Membranes were washed 3x10 min in PBST and then incubated with the secondary antibodies 1h at RT. Membranes were washed again 3x10 min in PBST and a last wash in PBS prior image acquisition with an Odyssey CLx Infrared Imaging system. For HRP-conjugated secondary antibodies, the membranes were developed using the ECL kit and scanned with ChemiDoc MP Imaging system (Bio-Rad). The blots were quantified with Image Studio Lite software and GraphPad Prism were used for statistical analysis (unpaired t test) of the data.

Whole-mount in situ hybridization (WM-ISH)

Whole-mount in situ hybridizations for snx10a and snx10b were performed as previously described (Thisse and Thisse, 2008) using digoxigenin-labelled riboprobes. Primer sequences for snx10a sense and antisense probes were; ATG probe: forward primer (5' ATGGATAACACAAGCTTTGAG3'), reverse primer (5'TCATATAACTGAATGGCCATG3') and for snx10b sense and antisense probes were; ATG probe: forward primer (5'TATGCAGGAATTCACTGGCG3'), reverse primer (5' CACTCTGATTCACATTGCAC3')

Zebrafish Maintenance

Wild-type zebrafish (AB strain) were housed at the zebrafish facility at the Centre for Molecular Medicine Norway (AVD.172) using standard practices. Embryos were incubated in egg water (0.06 g/L salt (Red Sea)) or E3 medium (5 mM NaCl, 0.17 mM KCl, 0.33 mM CaCl2, 0.33 mM MgSO4, equilibrated to pH 7.0). Embryos were held at 28 °C in an incubator following collection. Experimental procedures followed the recommendations of the Norwegian Regulation on Animal Experimentation ("Forskrift om forsøk med dyr" from 15.jan.1996). All experiments conducted on wild-type zebrafish larvae were done at 5 dpf or earlier.

CRISPR/Cas9 genome editing in zebrafish

Zebrafish snx10a and snx10b knock-out embryos were generated using CRISPR/Cas9 technology as described (Kroll et al., 2021). Two guide RNAs were designed each for snx10a and snx10b respectively, based on predictions from the online sgRNA prediction web tool CHOPCHOP

(http://chopchop.cbu.uib.no/index.php). Genomic DNA sequences retrieved from Ensembl GRCz10 or z11 (http://uswest.ensembl.org/Danio_rerio/Info/Index) were used for the target site searches. The two guides, designated as sgRNA#1 and sgRNA#2, were predicted to target exon 2 and exon 3 of the snx10a gene and exon 1 and 3 of the snx10b gene respectively. sgRNA is the annealed product of a target specific element called the crRNA and trans-activating CRISPR element called tracrRNA (both of which are ordered from Integrated DNA technologies, IDT). 1 ul of each of these nucleotide elements were annealed together with 1.28 ul of duplex buffer in a thermocycler at 95 ^{o}C for 5 min. Post annealing, 1 ul of sgRNA and 1 ul of Cas9 nuclease (IDT) was incubated together in a thermocycler at 37 ^{o}C for 5 min. sgRNA assembled with Cas9 is RNP. snx10a RNP was pooled together with snx10b RNP to create a mix of snx10ab RNP to create double knock-outs. 1nl (267.5 pg) of this mix was injected in the yolk sac at the single cell stage before the cell inflated. Oligonucleotides used for snx10a sgRNA synthesis were sgRNA#1 (5'ACGGGAUCCUCAGGUUCACAGUUUUAGAGCUAUGCU3') and sgRNA#2 (GGGUUCCAAGGAGGAAGUUUGUUUUAGAGCUAUGCU); for snx10b sgRNA synthesis were sgRNA#1 (5' AGAAAUUGGAGCCCGUAUGGGUUUUAGAGCUAUGCU3') and sgRNA#2 (5' CAUGCCAGAAAUCUUCCUUCGUUUUAGAGCUAUGCU3'). TracrRNA used was (5'AAAAGCACCGACTCGGTGCCACTTTTTCAAGTTGATAACGGACTAGCCTTA TTTTAACTTGCTATTTCTAGCTCTAAAAC'3).

Zebrafish cryosectioning, cell death assay by TUNEL Staining, confocal microscopy and image analysis

Control and *snx10ab* double knock-out (DKO) zebrafish larvae were treated or not with 100 μM DMOG for 24 hrs in the absence or presence of 100 μM NAC for the last 6 hrs of DMOG treatment at 3 dpf. At experimental endpoints, larvae were washed once in embryo water and fixed with 4% PFA (in HEPES) at RT for 2 hours. Post fixation, larvae were washed three times in PBS. The larvae were then cryopreserved in a 2 mL tube in increasing amounts of sucrose in 0.1 M PBS with 0.01% sodium azide. Cryopreservation was done first in 15% sucrose solution for 1 hr at RT or up until larvae dropped to the bottom of the tube and then in 30% sucrose solution at 4 °C overnight with gentle shaking. Cryopreserved larvae were oriented in a cryomold (Tissue-Tek Cryomold, Sakura, Ref: 4565) with optimal cutting temperature compound (OCT compound, Tissue-Tek Sakura, Ref: 4583). Larvae were oriented with the ventral side down, and additional OCT was added to fill the mold and frozen on dry ice. A solid block of OCT with larvae oriented in

the desired way was taken out from the mold and 12-µm coronal slices were sectioned on a cryostat (Thermo Scientific). Sections were collected on Superfrost Plus glass slides (Thermo Scientific, Ref: J1800AMNZ) and kept at RT for at least 2 hrs to firmly tether slices onto the glass slide.

Slides were rehydrated three times in PBS at room temperature for 3 min each. The area of interest was circled by a hydrophobic PAP pen (Abcam, ab2601), and the slides were placed in a humidified chamber to avoid drying out. Rest of the procedure for TUNEL staining (Terminal deoxynucleotidyl transferase-mediated deoxyUridine triphosphate Nick-End Labeling; Thermo Fisher Scientific) was performed according to the manufacturer's instructions. Confocal images were obtained using an Apochromat ×20/0.8 or ×40/1.0 oil DIC objective on an LSM 800 microscope (Zeiss). Image analysis was performed using Fiji by which mean fluorescent intensity was measured in the brain region of the respective sections of zebrafish larvae.

ROS analysis in Zebrafish

The analysis of reactive oxygen species (ROS) levels in zebrafish was performed as described [57]. Briefly, after dissociation into single cells of the respective larvae, cells were treated with 5 µM of MitoSOX (Thermo Fisher Scientific) in Hanks Balanced Salt Solution (HBSS) for 15 min at 28 °C in the dark. Cells were then centrifuged for 5 min at 250 x g at 4 °C, the supernatant discarded, and the cells washed with HBSS. FACS estimations were done on NovoCyte Flow Cytometer Systems, using an excitation peak of 396 nm for selective detection of mito superoxide.

Statistics

Experimental values were used for statistical analysis using Prism (v8.0.1) where indicated using analyses and post-hoc tests as indicated in figure legends. All data values come from distinct samples. * = $p < 0.05$, ** = $p < 0.01$, *** = $p < 0.001$, **** = $p < 0.0001$, non-significant differences are not depicted.

Online Supplemental material

Fig. S1 shows additional data for Fig. 1. Fig. S2 shows additional data for Fig. 5 and 6. Fig. S3 shows additional data for Fig. 7. Fig. S4 shows additional data for Fig. 9. Table S1 includes plasmids used in this study. Movie 1 is the time-lapse video of the data shown in Fig. 3C.

Data availability

All data used in this study are available upon request.

Acknowledgements:

We would like to thank the Simonsen lab for their support and critical discussion throughout the project development, especially Patricia González-Rodríguez for providing the U2OS Su9-HaloTag7-mGFP cells and Laura Rodriguez de la Ballina for the assistance with data analysis. We would like to acknowledge Ulrikke Dahl Brinch for assistance with EM sample preparation. We acknowledge the Norwegian Core Facility for Human Pluripotent Stem Cells at the Norwegian Center for Stem Cell Research for mycoplasma testing and the ALM core facility, Gaustad node, where high-content imaging was performed. Mass spectrometry-based proteomic analyses were performed by the Proteomics Core Facility, Department of Immunology, University of Oslo/Oslo University Hospital, which is supported by the Core Facilities program of the South-Eastern Norway Regional Health Authority. This core facility is also a member of the National Network of Advanced Proteomics Infrastructure (NAPI), which is funded by the Research Council of Norway INFRASTRUKTUR-program (project number: 295910). This project was carried out with funding from the Norwegian Cancer Society (grants no. 171318 and 223278), from the European Union's Horizon 2020 research and innovation program under the Marie Skłodowska-Curie (grant no. 801133), the South-Eastern Norway Regional Health Authority (grant no. 2020032) and the Research Council of Norway through its Centers of Excellence funding scheme (grant no. 262652) and FRIPRO (grant no. 249753). The authors declare no competing financial interests

Author contributions: Laura Trachsel-Moncho and Anne Simonsen designed and conceptualized the research project. Anne Simonsen supervised the work. Laura Trachsel-Moncho and Chiara Veroni carried out most in vitro experiments. Nagham Theres Asp contributed performing experiments. Benan John Mathai Performed all *Danio rerio* experiments. Ana Lapao and Serhiy Pankiv contributed to cloning design and molecular biology. Sakshi Singh analyzed mass spectrometry and proteomics data. Sebastian W. Schultz performed the electron microscopy experiments. Laura Trachsel-Moncho, Chiara Veroni and Anne Simonsen analyzed the data and wrote the manuscript.

References

Abuaita, Basel H., Tracey L. Schultz, and Mary X. O'Riordan. 2018. 'Mitochondria-Derived Vesicles Deliver Antimicrobial Reactive Oxygen Species to Control Phagosome-Localized Staphylococcus Aureus'. *Cell Host and Microbe* 24 (5): 625-636.e5. https://doi.org/10.1016/j.chom.2018.10.005.

Abudu, Yakubu Princely, Birendra Kumar Shrestha, Wenxin Zhang, Anthimi Palara, Hanne Britt Brenne, Kenneth Bowitz Larsen, Deanna Lynn Wolfson, et al. 2021. 'SAMM50 Acts with P62 in Piecemeal Basal- and OXPHOS-Induced Mitophagy of SAM and MICOS Components'. *The Journal of Cell Biology* 220 (8). https://doi.org/10.1083/JCB.202009092.

Allen, George F G, Rachel Toth, John James, and Ian G Ganley. 2013. 'Loss of Iron Triggers PINK1/Parkin-Independent Mitophagy.' *EMBO Reports* 14 (12): 1127–35. https://doi.org/10.1038/embor.2013.168.

Amirfiroozy, Akbar, Amir A Hamidieh, Zahra Golchehre, Azim Rezamand, Mahin Yahyaei, Fatemeh Beiranvandi, Soheyla Amirfiroozy, and Mohammad Keramatipour. 2017. 'A Novel Mutation in SNX10 Gene Causes Malignant Infantile Osteopetrosis.' *Avicenna Journal of Medical Biotechnology* 9 (4): 205–8.

Baechler, Brittany L., Darin Bloemberg, and Joe Quadrilatero. 2019. 'Mitophagy Regulates Mitochondrial Network Signaling, Oxidative Stress, and Apoptosis during Myoblast Differentiation'. *Autophagy* 15 (9): 1606–19. https://doi.org/10.1080/15548627.2019.1591672.

Bago, Ruzica, Nazma Malik, Michael J. Munson, Alan R. Prescott, Paul Davies, Eeva Sommer, Natalia Shpiro, et al. 2014. 'Characterization of VPS34-IN1, a Selective Inhibitor of Vps34, Reveals That the Phosphatidylinositol 3-Phosphate-Binding SGK3 Protein Kinase Is a Downstream Target of Class III Phosphoinositide 3-Kinase'. *Biochemical Journal* 463 (3): 413–27. https://doi.org/10.1042/BJ20140889.

Bao, Weilian, Yan You, Jiahui Ni, Hui Hou, Jiaren Lyu, Guize Feng, Yirui Wang, et al. 2023. 'Inhibiting Sorting Nexin 10 Promotes Mucosal Healing through SREBP2-Mediated Stemness Restoration of Intestinal Stem Cells'. *Science Advances* 9 (35). https://doi.org/10.1126/sciadv.adh5016.

Chandra, Mintu, Yanni K.Y. Chin, Caroline Mas, J. Ryan Feathers, Blessy Paul, Sanchari Datta, Kai En Chen, et al. 2019. 'Classification of the Human Phox Homology (PX) Domains Based on Their Phosphoinositide Binding Specificities'. *Nature Communications* 10 (1). https://doi.org/10.1038/s41467-019-09355-y.

Chen, Yanqun, Bin Wu, Liangliang Xu, Huapeng Li, Jianhong Xia, Wenguang Yin, Zhuo Li, et al. 2012. 'A SNX10/V-ATPase Pathway Regulates Ciliogenesis in Vitro and in Vivo'. *Cell Research* 22 (2): 333–45. https://doi.org/10.1038/cr.2011.134.

Cox, Jürgen, and Matthias Mann. 2008. 'MaxQuant Enables High Peptide Identification Rates, Individualized p.p.b.-Range Mass Accuracies and Proteome-Wide Protein Quantification'. *Nature Biotechnology* 26 (12): 1367–72. https://doi.org/10.1038/nbt.1511.

Das, Anupam, Sagarika Nag, Anne B. Mason, and Margarida M. Barroso. 2016. 'Endosome-Mitochondria Interactions Are Modulated by Iron Release from Transferrin'. *Journal of Cell Biology* 214 (7): 831–45. https://doi.org/10.1083/jcb.201602069.

Deng, Rong rong, and You ping Yuan. 2024. 'Ropivacaine Inhibits the Proliferation and Metastasis of Gastric Cancer Cells via the SNX10/SRC/STAT3 Pathway'. *Chemical Biology and Drug Design* 103 (1): 1–10. https://doi.org/10.1111/cbdd.14405.

Elson, Ari, Merle Stein, Grace Rabie, Maayan Barnea-Zohar, Sabina Winograd-Katz, Nina Reuven, Moran Shalev, et al. 2021. 'Sorting Nexin 10 as a Key Regulator of Membrane Trafficking in Bone-Resorbing Osteoclasts: Lessons Learned From Osteopetrosis'. *Frontiers in Cell and Developmental Biology* 9 (May): 1–17. https://doi.org/10.3389/fcell.2021.671210.

Feng, Hui, Jiani Tan, Qijuan Wang, Tingting Zhou, Liu Li, Dongdong Sun, Minmin Fan, Haibo Cheng, and Weixing Shen. 2023. 'α-Hederin Regulates Glucose Metabolism in Intestinal Epithelial Cells by Increasing SNX10 Expression'. *Phytomedicine* 111:154677. https://doi.org/10.1016/j.phymed.2023.154677.

Feng, Yuchen, Ding He, Zhiyuan Yao, and Daniel J Klionsky. 2014. 'The Machinery of Macroautophagy.' *Cell Research* 24 (1): 24–41. https://doi.org/10.1038/cr.2013.168.

Gimple, Ryan C., Guoxin Zhang, Shuai Wang, Tengfei Huang, Jina Lee, Suchet Taori, Deguan Lv, et al. 2023. 'Sorting Nexin 10 Sustains PDGF Receptor Signaling in Glioblastoma Stem Cells via Endosomal Protein Sorting'. *JCI Insight* 8 (6): 1–25. https://doi.org/10.1172/jci.insight.158077.

Guerroué, François Le, Franziska Eck, Jennifer Jung, Tatjana Starzetz, Michel Mittelbronn, Manuel Kaulich, and Christian Behrends. 2017. 'Autophagosomal Content Profiling Reveals an LC3C-Dependent Piecemeal Mitophagy Pathway'. *Molecular Cell* 68 (4): 786-796.e6. https://doi.org/10.1016/J.MOLCEL.2017.10.029.

Hamdi, Amel, Tariq M. Roshan, Tanya M. Kahawita, Anne B. Mason, Alex D. Sheftel, and Prem Ponka. 2016. 'Erythroid Cell Mitochondria Receive Endosomal Iron by a "Kiss-and-Run" Mechanism'. *Biochimica et Biophysica Acta - Molecular Cell Research* 1863 (12): 2859–67. https://doi.org/10.1016/j.bbamcr.2016.09.008.

Hammerling, Babette C., Rita H. Najor, Melissa Q. Cortez, Sarah E. Shires, Leonardo J. Leon, Eileen R. Gonzalez, Daniela Boassa, et al. 2017. 'A Rab5 Endosomal Pathway Mediates Parkin-Dependent Mitochondrial Clearance'. *Nature Communications* 8. https://doi.org/10.1038/ncomms14050.

Hansen, Grace T., Débora R. Sobreira, Zachary T. Weber, Alexis G. Thornburg, Ivy Aneas, Li Zhang, Noboru J. Sakabe, et al. 2023. 'Genetics of Sexually Dimorphic Adipose Distribution in Humans'. *Nature Genetics* 55 (3): 461–70. https://doi.org/10.1038/s41588-023-01306-0.

Heberle, Henry, Vaz G. Meirelles, Felipe R. da Silva, Guilherme P. Telles, and Rosane Minghim. 2015. 'InteractiVenn: A Web-Based Tool for the Analysis of Sets through Venn Diagrams'. *BMC Bioinformatics* 16 (1): 1–7. https://doi.org/10.1186/s12859-015-0611-3.

Holehouse, Alex S, and Birthe B Kragelund. 2023. 'The Molecular Basis for Cellular Function of Intrinsically Disordered Protein Regions'. *Nature Reviews Molecular Cell Biology*. https://doi.org/10.1038/s41580-023-00673-0.

Hyttinen, Juha M.T., Minna Niittykoski, Antero Salminen, and Kai Kaarniranta. 2013. 'Maturation of Autophagosomes and Endosomes: A Key Role for Rab7'. *Biochimica et Biophysica Acta (BBA) - Molecular Cell Research* 1833 (3): 503–10. https://doi.org/10.1016/J.BBAMCR.2012.11.018.

Jumper, John, Richard Evans, Alexander Pritzel, Tim Green, Michael Figurnov, Olaf Ronneberger, Kathryn Tunyasuvunakool, et al. 2021. 'Highly Accurate Protein Structure Prediction with AlphaFold'. *Nature* 596 (7873): 583–89. https://doi.org/10.1038/s41586-021-03819-2.

Koçak, Gamze, Banu Nur Güzel, Ercan Mıhçı, Osman Alphan Küpesiz, Koray Yalçın, and Ayşe Esra Manguoğlu. 2019. 'TCIRG1 and SNX10 Gene Mutations in the Patients with Autosomal Recessive Osteopetrosis'. *Gene* 702:83–88. https://doi.org/10.1016/j.gene.2019.02.088.

Kremer, James R., David N. Mastronarde, and J. Richard McIntosh. 1996. 'Computer Visualization of Three-Dimensional Image Data Using IMOD'. *Journal of Structural Biology* 116 (1): 71–76. https://doi.org/10.1006/JSBI.1996.0013.

Lee, Wonseok, Hyun Young Kim, You Jin Choi, Seung Hwan Jung, Yoon Ah Nam, Yunfan Zhang, Sung Ho Yun, Tong Shin Chang, and Byung Hoon Lee. 2022. 'SNX10-Mediated Degradation of LAMP2A by NSAIDs Inhibits Chaperone-Mediated Autophagy and Induces Hepatic Lipid Accumulation'. *Theranostics* 12 (5): 2351–69. https://doi.org/10.7150/THNO.70692.

Lin, Qisheng, Shu Li, Na Jiang, Xinghua Shao, Minfang Zhang, Haijiao Jin, Zhen Zhang, et al. 2019. 'PINK1-Parkin Pathway of Mitophagy Protects against Contrast-Induced Acute Kidney Injury via Decreasing Mitochondrial ROS and NLRP3 Inflammasome Activation'. *Redox Biology* 26 (May): 101254. https://doi.org/10.1016/j.redox.2019.101254.

Liu, Jialing, Zhonghua Gao, and Xiangjie Liu. 2024. 'Mitochondrial Dysfunction and Therapeutic Perspectives in Osteoporosis'. *Frontiers in Endocrinology* 15. https://doi.org/10.3389/FENDO.2024.1325317.

Lou, Jun, Xiawei Li, Wei Huang, Jingjing Liang, Mingzhu Zheng, Ting Xu, Jun Lyu, et al. 2017. 'SNX10 Promotes Phagosome Maturation in Macrophages and Protects Mice against Listeria Monocytogenes Infection'. *Oncotarget* 8 (33): 53935–47. https://doi.org/10.18632/oncotarget.19644.

Ma, Lixiu, Tianyu Han, and Yi-an Zhan. 2024. 'Mechanism and Role of Mitophagy in the Development of Severe Infection'. *Cell Death Discovery* 10 (1): 88. https://doi.org/10.1038/s41420-024-01844-4.

Melia, Thomas J., Alf H. Lystad, and Anne Simonsen. 2020. 'Autophagosome Biogenesis: From Membrane Growth to Closure'. *Journal of Cell Biology*. Rockefeller University Press. https://doi.org/10.1083/JCB.202002085.

Munson, Michael J., Benan J. Mathai, Matthew Yoke Wui Ng, Laura Trachsel-Moncho, Laura R. de la Ballina, Sebastian W. Schultz, Yahyah Aman, et al. 2021. 'GAK and PRKCD Are Positive Regulators of PRKN-Independent Mitophagy'. *Nature Communications 2021 12:1* 12 (1): 1–22. https://doi.org/10.1038/s41467-021-26331-7.

Pangrazio, Alessandra, Anders Fasth, Andrea Sbardellati, Paul J Orchard, Kimberly A Kasow, Jamal Raza, Canan Albayrak, et al. 2013. '*SNX10* Mutations Define a Subgroup of Human Autosomal Recessive Osteopetrosis with Variable Clinical Severity'. *Journal of Bone and Mineral Research* 28 (5): 1041–49. https://doi.org/10.1002/jbmr.1849.

Pankiv, Serhiy, Anette Kathinka Dahl, Aleksander Aas, Rosa Linn Andersen, Andreas Brech, Petter Holland, Sakshi Singh, Christian Bindesbøll, and Anne Simonsen. 2024. 'BEACH Domain Proteins Function as Cargo-Sorting Adaptors in Secretory and Endocytic Pathways'. *The Journal of Cell Biology* 223 (12). https://doi.org/10.1083/JCB.202408173.

Perez-Riverol, Yasset, Jingwen Bai, Chakradhar Bandla, David García-Seisdedos, Suresh Hewapathirana, Selvakumar Kamatchinathan, Deepti J. Kundu, et al. 2022. 'The PRIDE Database Resources in 2022: A Hub for Mass Spectrometry-Based Proteomics Evidences'. *Nucleic Acids Research* 50 (D1): D543. https://doi.org/10.1093/NAR/GKAB1038.

Petherick, Katy J., Owen J.L. Conway, Chido Mpamhanga, Simon A. Osborne, Ahmad Kamal, Barbara Saxty, and Ian G. Ganley. 2015. 'Pharmacological Inhibition of ULK1 Kinase Blocks Mammalian Target of Rapamycin (MTOR)-Dependent Autophagy'. *Journal of Biological Chemistry* 290 (18): 11376–83. https://doi.org/10.1074/jbc.C114.627778.

Prashar, Akriti, Claudio Bussi, Antony Fearns, Mariana I. Capurro, Xiaodong Gao, Hiromi Sesaki, Maximiliano G. Gutierrez, and Nicola L. Jones. 2024. 'Lysosomes Drive the Piecemeal Removal of Mitochondrial Inner Membrane'. *Nature* 632 (8027): 1110–17. https://doi.org/10.1038/S41586-024-07835-W.

Princely Abudu, Yakubu, Serhiy Pankiv, Benan John Mathai, Alf Håkon Lystad, Christian Bindesbøll, Hanne Britt Brenne, Matthew Yoke Wui Ng, et al. 2019. 'NIPSNAP1 and NIPSNAP2 Act as "Eat Me" Signals for Mitophagy'. *Developmental Cell* 49 (4): 509-525.e12. https://doi.org/10.1016/j.devcel.2019.03.013.

Qin, Baoming, Miao He, Xiao Chen, and Duanqing Pei. 2006. 'Sorting Nexin 10 Induces Giant Vacuoles in Mammalian Cells.' *The Journal of Biological Chemistry* 281 (48): 36891–96. https://doi.org/10.1074/jbc.M608884200.

Ritchie, Matthew E., Belinda Phipson, Di Wu, Yifang Hu, Charity W. Law, Wei Shi, and Gordon K. Smyth. 2015. 'Limma Powers Differential Expression Analyses for RNA-Sequencing and Microarray Studies'. *Nucleic Acids Research* 43 (7): e47. https://doi.org/10.1093/nar/gkv007.

Rusten, Tor Erik, and Harald Stenmark. 2009. 'How Do ESCRT Proteins Control Autophagy?' *Journal of Cell Science* 122 (13): 2179–83. https://doi.org/10.1242/jcs.050021.

Sheftel, Alex D., An Sheng Zhang, Claire Brown, Orian S. Shirihai, and Prem Ponka. 2007. 'Direct Interorganellar Transfer of Iron from Endosome to Mitochondrion'. *Blood* 110 (1): 125–32. https://doi.org/10.1182/blood-2007-01-068148.

Shepherd, D., and P. B. Garland. 1969. 'The Kinetic Properties of Citrate Synthase from Rat Liver Mitochondria.' *The Biochemical Journal* 114 (3): 597–610. https://doi.org/10.1042/bj1140597.

Shutt, Timothy E., and Heidi M. McBride. 2013. 'Staying Cool in Difficult Times: Mitochondrial Dynamics, Quality Control and the Stress Response'. *Biochimica et Biophysica Acta - Molecular Cell Research* 1833 (2): 417–24. https://doi.org/10.1016/j.bbamcr.2012.05.024.

Simonsen, Anne, Roger Lippé, Savvas Christoforidis, Jean Michel Gaullier, Andreas Brech, Judy Callaghan, Ban Hock Toh, Carol Murphy, Marino Zerial, and Harald Stenmark. 1998. 'EEA1 Links PI(3)K Function to Rab5 Regulation of Endosome Fusion'. *Nature* 394 (6692): 494–98. https://doi.org/10.1038/28879.

Soubannier, Vincent, Gian Luca McLelland, Rodolfo Zunino, Emelie Braschi, Peter Rippstein, Edward A. Fon, and Heidi M. McBride. 2012. 'A Vesicular Transport Pathway Shuttles Cargo from Mitochondria to Lysosomes'. *Current Biology : CB* 22 (2): 135–41. https://doi.org/10.1016/J.CUB.2011.11.057.

Stattin, Eva-Lena, Petra Henning, Joakim Klar, Emma McDermott, Christina Stecksen-Blicks, Per-Erik Sandström, Therese G. Kellgren, et al. 2017. 'SNX10 Gene Mutation Leading to Osteopetrosis with Dysfunctional Osteoclasts'. *Scientific Reports* 7 (1): 3012. https://doi.org/10.1038/s41598-017-02533-2.

Stirling, David R., Madison J. Swain-Bowden, Alice M. Lucas, Anne E. Carpenter, Beth A. Cimini, and Allen Goodman. 2021. 'CellProfiler 4: Improvements in Speed, Utility and Usability'. *BMC Bioinformatics* 22 (1): 1–11. https://doi.org/10.1186/S12859-021-04344-9/FIGURES/6.

Team, R Core. 2020. 'R: The R Project for Statistical Computing'. Vienna, Austria. 2020. https://www.r-project.org/.

Tyanova, Stefka, Tikira Temu, Pavel Sinitcyn, Arthur Carlson, Marco Y. Hein, Tamar Geiger, Matthias Mann, and Jürgen Cox. 2016. 'The Perseus Computational Platform for Comprehensive Analysis of (Prote)Omics Data'. *Nature Methods*. Nature Publishing Group. https://doi.org/10.1038/nmeth.3901.

Vagnozzi, Alana N., and Domenico Praticò. 2019. 'Endosomal Sorting and Trafficking, the Retromer Complex and Neurodegeneration'. *Molecular Psychiatry*. Nature Publishing Group. https://doi.org/10.1038/s41380-018-0221-3.

Varadi, Mihaly, Stephen Anyango, Mandar Deshpande, Sreenath Nair, Cindy Natassia, Galabina Yordanova, David Yuan, et al. 2022. 'AlphaFold Protein Structure Database: Massively Expanding the Structural Coverage of Protein-Sequence Space with High-Accuracy Models'. *Nucleic Acids Research* 50 (D1): D439–44. https://doi.org/10.1093/nar/gkab1061.

Wen-You Yim, Willa, Hayashi Yamamoto, and Noboru Mizushima. 2022. 'A Pulse-Chasable Reporter Processing Assay for Mammalian Autophagic Flux with HaloTag'. *ELife* 11. https://doi.org/10.7554/ELIFE.78923.

Yamano, Koji, Chunxin Wang, Shireen A. Sarraf, Christian Münch, Reika Kikuchi, Nobuo N. Noda, Yohei Hizukuri, et al. 2018. 'Endosomal Rab Cycles Regulate Parkin-Mediated Mitophagy'. *ELife* 7. https://doi.org/10.7554/eLife.31326.

You, Yan, Wan Zhen Li, Sulin Zhang, Bin Hu, Yue Xuan Li, Hai Dong Li, Huan Huan Tang, et al. 2018. 'SNX10 Mediates Alcohol-Induced Liver Injury and Steatosis by Regulating the Activation of Chaperone-Mediated Autophagy'. *Journal of Hepatology* 69 (1): 129–41. https://doi.org/10.1016/j.jhep.2018.01.038.

You, Yan, Chun Zhou, Dong Li, Zhong-Lian Cao, Weixing Shen, Wan-Zhen Li, Sulin Zhang, Bin Hu, and Xiaoyan Shen. 2016. 'Sorting Nexin 10 Acting as a Novel Regulator of Macrophage Polarization Mediates Inflammatory Response in Experimental Mouse Colitis'. *Scientific Reports* 6 (1): 20630. https://doi.org/10.1038/srep20630.

Author notes

Disclosures: The authors declare no competing interests exist.

Figure legends

Figure 1. SNX10 localizes to early and late endocytic compartments

A) Graphical view of the SNX10 isoforms annotated in UniProt. The PX domain is represented in green, and the numbers indicate the number or amino acids. The arrows indicate the position of the natural variants (SNPs) linked to ARO (Y32S, R51P, R51Q). **B)** The figure displays the predicted protein structure of SNX10 generated using AlphaFold, showcasing its three-dimensional conformation. **C)** Confocal imaging of U2OS cell lines stably expressing doxycycline inducible SNX10-EGFP WT or the indicated ARO-linked mutants. Nuclei were stained with Hoechst. Scale bar: 20 µm. **D)** Representative immunoblot showing the expression levels of SNX10-EGFP and the indicated ARO mutants. The membrane was blotted using an antibody anti-GFP and using Actin as loading control. **E)** Representative immunofluorescence images of U2OS cells stably expressing SNX10-EGFP WT or the Y32S mutant (green) immuno-stained with anti-EEA1 (magenta) after treating cells with 5µM VPS34-IN1 for 2 hrs. Nuclei were stained with Hoechst. Scale bar: 10 µm. Insets: 9.35x9.35 µm **F)** Representative image of U2OS cells stably expressing SNX10-EGFP and immunostained with anti-CD63 (magenta) and anti-EEA1 (yellow) antibodies. Images were taken with a Nikon CREST X-Light V3 spinning disk microscope using a 60x oil objective (NA 1.42). Scale bar: 10 µm. Insets: 5.12x5.12 µm. **G)** Quantification of F) represented as percentage of SNX10 structures that are either CD63- or EEA1-positive. Data are mean ± SEM with individual data points corresponding to a single field of view (n > 300 cells, four experiments). The significance was assessed by unpaired t-test. Data distribution was assumed to be normal, but this was not formally tested. **H)** Representative immunofluorescence images of U2OS cells stably expressing SNX10-EGFP WT or the Y32S mutant (green) immuno-stained with anti-LAMP1. Scale bar: 10 µm. Insets: 10.43x10.43 µm **I)** U2OS SNX10-EGFP cells fixed for CLEM analysis. The area analyzed and shown in (ii) is indicated with a square in the confocal image (i). (iii) shows the transmission EM and (iv) the z-slide from the tomogram from the white dotted area shown in (ii). The white arrows indicate clathrin-coated vesicles. (v) green: endosomes; red: lipid droplets; yellow: vesicles; and pink: clathrin-coated vesicles. Scale bars: 10 µm (i and ii), 1 µm (iii and iv).

Figure 2. SNX10 regulates endocytic trafficking

A) Graphical description of the plasma membrane EGFR staining. Live cells are put on ice, and (1) incubated for 20 min with the primary anti-EGFR antibody, then washed and (2) incubated with a secondary antibody for 20 min, followed by (3) incubation with EGF for 15 or 50 min at 37ºC before fixation and imaging. **B)** U2OS SNX10-EGFP cells were incubated with anti-EGFR antibody as described in A), then stimulated with EGF and fixed. Cells were stained with an anti-EFG

antibody after fixation. Scale bar: 10 µm. Insets: 7.24x7.24 µm. **C)** After 72 hrs of siRNA transfection, U2OS cells were serum starved for 2 hrs and then incubated with 50 ng/ml EGF + 10 µg/ml Cycloheximide (CHX) for the indicated times. The cells were lysed followed by western blotting for the indicated proteins. **D)** Quantification of EGFR protein levels normalized to Actin in n= 3 independent experiments ± SEM. Significance was determined by two-way ANOVA followed by Tukey's multiple comparisons test. Normality was assumed but not formally tested. **E)** Cells were reverse transfected with 20nM siRNA: siCtrl (control) and two different siSNX10 oligoes (siSNX10#1 and siSNX10#2) prior to fixation and staining for endogenous EEA1. Images were taken with Zeiss Axio Observer widefield microscope (Zen Blue 2.3, Zeiss) and a 20x objective was used. Scale bar: 10 µm. **F)** Quantification of the data shown in E) was performed using CellProfiler software. The values were obtained from analyzing >1000 cells per condition and they were normalized to control siRNA (siCtrl). The graphs display the mean values ± SEM from n = 3 independent experiments. The significance was assessed by ordinary one-way ANOVA followed by Bonferroni's post hoc test. Data distribution was assumed to be normal but was not formally tested. **G)** Representative electron microscopy images of endosomes in U2OS cells (control and siSNX10 #1). Pink arrows: Protein A conjugated with 10 nm gold (PAG10) labeling EGFR that has been taken up into endosomes, Yellow arrows: endosome not containing internalized PAG10-labeled EGFR. Scale bar: 0.5 µm **H)** Measurements of EGFR-containing endosome diameter in control vs siSNX10 treated cells from one experiment. The graph shows the endosomal diameter (nm) of a total 24 PAG10-labeled EGFR endosomes in siCtrl cells and 15 PAG10-labeled EGFR endosomes in siSNX10 cells. The graph displays the mean values ± SEM. Significance was determined by unpaired t-test with Welch's correction in all graphs and data distribution was assumed to be normal but was not formally tested. * = $p < 0.05$, ** = $p < 0.01$, non-significant differences are not depicted.

Figure 3. SNX10 localizes nearby mitochondria

A) SNX10-EGFP WT or the Y32S mutant, stably expressed in U2OS cells, underwent GFP pulldown for the subsequent analysis of their interactome using mass spectrometry assays. A total of 53 proteins were identified as significant SNX10-EGFP interactors compared to the EGFP control, as analyzed by R lima using a cut-off value of log2FC > 1 and adjusted P-value < 0.05. The Venn diagram illustrates the distinct and shared interactors between the SNX10 WT and Y32S mutant, where the identified significant SNX10-EGFP interacting proteins are listed below. **B)** The

interacting proteins of SNX10 WT were enriched for GO term analysis. The enrichment of the Cellular Component they belong to (pie chart above) and Biological Processes they are involved in (pie chart below) is expressed in percentage towards the significant hits. Graphs were plotted using plotly (python package). **C)** U2OS with stable inducible expression of SNX10-EGFP were treated with doxycycline for 24 hrs before incubation with MitoTracker Red for 30 min, followed by live imaging with an acquisition speed of 1 frame every 500 ms. Scale bar: 10 µm. **D)** U2OS cells stably expressing mScarlet-RAB5 and with inducible expression of SNX10-EGFP were stained with MitoTracker Deep Red FM in the presence or absence of DFP (1 µM). Scale bar: 10 µm. **E)** U2OS SNX10-EGFP cells were treated with or without DFP (1 µM) for 24 hrs and with or without MRT68921 (1 µM) for 1 hr. MitoTracker Deep Red FM (100 nM) was added for 1 hr, followed by immunofluorescence staining with antibody against LC3B. Scale bars: 10 µm. Insets 5.77x5.77 µm **F and G)** Quantification of the percentage of the co-occurrence of LC3 on SNX10 structures F) and of LC3 on Mitrotracker-SNX10-positive structures G). Data are mean ± SEM with individual data points corresponding to a single field of view (n=4 (F) and n=3 (G), corresponding experiment shown in the same colour, >150 cells per experiment). The statistical significance was calculated with ordinary one-way ANOVA, followed by Tukey's multiple comparison test. Data distribution was assumed to be normal, but this was not formally tested. * = $p < 0.05$, ** = $p < 0.01$, *** = $p < 0.001$, **** = $p < 0.0001$, non-significant differences are not depicted.

Figure 4. SNX10 structures containing mitochondria mature into late endosomes

U2OS cells with inducible expression of SNX10-EGFP were treated with DFP (1 µM) or DMOG (1 µM) for 24 hrs, stained with MitoTracker Deep Red FM (100 nM) for 30 minutes, followed by immunofluorescence with antibodies anti-LC3B and anti-EEA1 **A)** or anti-CD63 **C)**, prior to acquisition with a Nikon CREST X-Light V3 spinning disk microscope using a 60x oil objective (NA 1.42). Scale bar: 10 µm. Insets: 5.52x5.52 µm (A), 6.62x6.62 µm (C). **B-D)** Pixel intensity plots for line in Control, DFP, and DMOG insets, respectively for A) and C).

Figure 5. SNX10 vesicles contain mitochondrial proteins and LC3B

A) U2OS cells with stable inducible expression of SNX10-EGFP were pre-treated with doxycycline for 16 hrs before the addition of DFP (1 µM) for 24 hrs. The cells were fixed and stained with antibodies against mitochondrial proteins. Scale bars: 10 µm. Insets: 8.57x8.57 µm **B)** U2OS cells with inducible expression of SNX10-EGFP were treated with DFP (1 µM) or DMOG (1 µM) for 24

hrs and stained with antibodies anti-COX-IV and anti-LC3B in B) or anti-LAMP1 in D), prior to acquisition with a Nikon CREST X-Light V3 spinning disk microscope using a 60x oil objective (NA 1.42). Scale bar: 10 µm. Insets: 4.41x4.41 µm (B), 5.52x5.52 µm (D). **C-E)** Pixel intensity plots for line in Control, DFP and DMOG insets, respectively for B) and D).

Figure 6. SNX10 is a negative regulator of COX-IV turnover

A) U2OS cells were reverse transfected with the indicated siRNA (20 nM) for 72 hrs, then treated or not with DFP (1 µM) for 24 hrs and with BafA1 (50 nM) the last 16 hrs, followed by western blotting for the indicated proteins. **B-D)** Quantification of the data in A) from n=5, 3 and 6 independent experiments. Bars show mean values of the protein levels normalized to Actin relative to Control conditions (siCtrl Control) ± SEM. Significance is assessed by two-way ANOVA followed by Tukey's post hoc test. Data distribution was assumed to be normal. **E)** U2OS cells with stable expression of mScarlet-RAB5 were reverse transfected with the indicated siRNA (20 nM) for 72 hrs, then treated or not with DFP for 24 hrs. The cells were fixed and stained with antibody anti-COX-IV, before acquisition. Scale bar: 10 µm. Insets: 3.69x3.69 µm. **F)** Quantification of COX-IV intensity from E) represented as z-score from 2 independent experiments (>250 cells per experiment). The statistical significance between the Control and the other conditions was calculated with ordinary one-way ANOVA followed by Tukey's multiple comparison test. Data distribution was assumed to be normal but was not formally tested. * = $p < 0.05$, ** = $p < 0.01$, *** = $p < 0.001$, **** = $p < 0.0001$, non-significant differences are not depicted.

Figure 7. SNX10 modulates piecemeal mitophagy of OXPHOS components

A) U2OS cells stably expressing the reporter pSu9-Halo-mGFP were seeded and subjected to knockdown for 72 hrs. Cells were treated with TMR (100 nM) for 20 min, washed three times with PBS, and then treated with DFP (1 µM), DMOG (1 µM), or left untreated (control) for 24 hrs before lysis. **B-C)** The relative Free Halo Tag expression was quantified using the formula (Free Halo / (Free Halo + Full Length)) normalized to Actin. Data in B) were Data in B) were log2-transformed. Statistical analysis was performed using one-way ANOVA followed by Dunnett's multiple comparison tests to compare treatment groups to the control. Data represent mean ± SEM from three independent experiments. Data distribution was assumed to be normal but was

not formally tested. **D)** U2OS cells with inducible expression of SNX10-EGFP were treated with or without DFP (1 µM) for 24 hrs and stained with antibodies anti-COX-IV and anti-p62, followed by acquisition with a Nikon Ti2-E microscope with a Yokogawa CSU-W1 SoRa spinning disk 100x/1.45 NA oil immersion objective. Pixel intensity plot line graphs from Control and DFP insets were generated with GraphPad Prism using two different y axis to enhance visualization. Scale bar: 10 µm. Insets: 4.08x4.08 µm **E)** U2OS cells subjected to reverse transfection with sip62 (20 nM) for 72 hrs were stained with an anti-COX-IV and anti-p62 antibody, prior to acquisition with a Nikon Ti2-E microscope with a Yokogawa CSU-W1 SoRa spinning disk 100x/1.45 NA oil immersion objective. 100x/1.45 NA oil immersion objective. Scale bar: 10 µm. **F)** Quantification of COX-IV intensity from E) represented as z-score from 1 experiment with individual data points corresponding to a single field of view (>30 cells per siRNA). Significance was determined by unpaired two-tailed t-test. Data distribution was assumed to be normal, but this was not formally tested. **G)** Representative images of U2OS cells subjected to reverse transfection with siSNX10 (20nM) for 72 hrs, followed by treatment with either IN1 or MRT for 24 hrs before fixation. Post-fixation, cells were stained with a COX-IV antibody, and images were captured using an ImageXpress Micro Confocal (Molecular Devices) at 20X magnification. **H-I)** Quantification of COX-IV intensity from G) represented as z-score from 1 independent experiment, with individual data points corresponding to a single field of view (>200 cells were analyzed for each condition). Significance was determined by one- ANOVA followed by Šídák's multiple comparisons test. Data distribution was assumed to be normal, but this was not formally tested. * = $p < 0.05$, ** = $p < 0.01$, *** = $p < 0.001$, **** = $p < 0.0001$, non-significant differences are not depicted.

Figure 8. SNX10 is important for mitochondrial bioenergetics

A) Mitochondrial oxygen consumption rate (OCR) was assessed in control and SNX10 knocked down cells using the Seahorse XFe24 Analyzer. OCR was measured following sequential addition of Oligomycin, carbonyl cyanide m-chlorophenyl hydrazone (CCCP), and Rotenone/Antimycin A (Rot/AntiA). **B)** The four basal OCR measurements per well were averaged to determine the basal OCR value, and non-mitochondrial respiration was subtracted to ascertain the basal respiration associated with each condition. **C)** ATP production was calculated by subtracting the proton leak from the maximal respiratory capacity. Error bars represent the mean ± SEM from n=5. Statistical significance was determined using one-way ANOVA followed by Dunnett's multiple comparison test. Data distribution was assumed to be normal but was not formally tested. **D)** Citrate Synthase

activity was determined by spectrophotometry from lysates of U2OS cells transfected with siRNA for 72 hrs, in the presence or absence of DFP for the last 24 hrs. The graph displays mean values normalized to siCtrl. Significance was determined from n = 3 independent experiments, by two-way ANOVA followed by Tukey's multiple comparison test. Data distribution was assumed to be normal but was not formally tested. **E-F)** Expression levels of citrate synthase were measured in control (siCtrl) and SNX10 knockdowns (siSXN10#1, siSXN10#2) across three independent experiments. Band densities of citrate synthase were normalized to the housekeeping gene GAPDH. Data are presented as mean ± SEM. Statistical analysis was performed using one-way ANOVA followed by Dunnett's post-hoc test to compare each knockdown group to the control group. Data distribution was assumed to be normal but was not formally tested. * = $p < 0.05$, ** = $p < 0.01$, *** = $p < 0.001$, **** = $p < 0.0001$, non-significant differences are not depicted.

Figure 9. SNX10 regulates mitochondrial homeostasis and cell death *in vivo*

A) Schematic diagram of human SNX10, zebrafish Snx10a and Snx10b proteins. The percentage identity of the orthologues amongst each other and to the human counterpart is indicated. Also, the percentage identity of the zebrafish PX domains in comparison with the PX domain of human SNX10 is shown. **B)** Temporal expression pattern of *snx10a* and *snx10b*. The graph shows the fold change in transcript levels relative to β-actin in whole zebrafish embryos from 1 dpf to 5 dpf. Error bars indicate mean ± SEM. Data is collected from 3 individual experiments using 30 larvae for each experiment. **C)** Dorsal and lateral view of the spatial expression pattern of *snx10a* and *snx10b* at 3 dpf as demonstrated by whole-mount in situ hybridization (WM-ISH) using an internal probe. Scale bars: 200 µm. Images are representative from 3 experiments. **D)** Representative immunoblots of Snx10 and β-tubulin on whole embryo lysates from control (scrambled guide), single *snx10a* and double *snx10ab* KO (DKO) animals. β-tubulin served as a loading control. **E)** Representative immunoblots of Snx10, Samm50, Cox-IV and Actin on whole embryo lysates from control (scrambled guide) and *snx10ab* DKO treated with 100 µM DMOG or DMSO control for 24 hrs at 2 dpf. **F)** Quantification of the Cox-IV signal intensity from blots in E) normalized to control DMSO signal intensity from n=4 experiments. Error bars indicate mean ± SEM, unpaired Students t-test was performed to assess significance. **G)** Quantification of the Samm50 signal intensity from blots in E) normalized to control DMSO signal intensity from n=4 experiments. Error bars indicate mean ± SEM, unpaired Students t-test was performed to assess significance. Data distribution was assumed to be normal but was not formally tested. **H)** Representative images

of TUNEL assay on control (scrambled sgRNA) and *snx10ab* DKO larvae treated with 100 µM DMOG or DMSO control for 24 hrs at 3 dpf. Orientation lateral. Scale bar: 500 µm. **I)** Quantification of the mean fluorescent intensity from demarcated brain regions of images in H). A total of 45 control larvae (scrambled sgRNA) and 41 *snx10ab* DKO larvae were used for quantification, respectively. Values were normalized to control DMSO values. Control larvae were treated with DMOG as a comparison to *snx10ab* DKO larvae. n = 2 independent experiments. Plots demonstrate data distribution and median value (red line). Significance was determined by two-way ANOVA followed by Tukey's post-test to compare all groups. Data distribution was assumed to be normal but was not formally tested. **J)** Quantification of ROS levels obtained via FACS analysis of control (scrambled sgRNA), *snx10ab* DKO and positive control larvae at 3 dpf incubated with MitoSOX. The values presented as relative values after normalizing to control. Error bars indicate mean ± SEM. Quantification was from at least 2 independent experiments. Data distribution was assumed to be normal but was not formally tested. **K)** Representative whole mount images shown as maximum intensity projection from z-stack of *TUNEL* assay performed on control (scrambled sgRNA) and *snx10ab* DKO larvae treated with or without 100 µM NAC at 3 dpf. Orientation lateral. Scale bar: 500 µm. **L)** Quantification of the number of white puncta (dots) from the demarcated whole brain region shown in K). A total of >20 control larvae (scrambled gRNA) and >20 *snx10ab* DKO larvae treated or not with 100 µM NAC were used for quantification. Values were normalized to control values. Data is collected from 3 individual experiments. Plots show data distribution and median value (red line). Significance was determined by one-way Brown-Forsythe and Welch's ANOVA test to compare all groups. Data distribution was assumed to be normal but was not formally tested. * = $p < 0.05$, ** = $p < 0.01$, *** = $p < 0.001$, **** = $p < 0.0001$, no significant differences are not depicted.

Figure 10. Model showing the role of SNX10 as a modulator of endocytic transport and piecemeal mitophagy

In vitro: under normal conditions (Control), SNX10 localizes to early endosomes (RAB5 and EEA1 positive) and late endosomes (CD63 positive) together with endocytic cargo (as EGFR). SNX10-positive structures are also observed near mitochondria. Upon hypoxia-mimicking conditions (induced by DFP or DMOG) SNX10 vesicles colocalize with CD63, LC3B and p62 and incorporate selected mitochondrial components (including COX-IV), indicating a role for SNX10 in selective mitochondrial degradation. Upon SNX10 knockdown (SNX10 KD), early endosomes appear

smaller and more numerous, with a corresponding reduced degradation of EGFR. In contrast, the turnover of mitochondrial COX-IV and ATP synthase is increased, along with reduced oxygen consumption rate and ATP production, reflecting impaired mitochondrial function. The arrow thicknesses indicate the extent of the different pathways under different conditions.

In vivo: in zebrafish larvae, *Snx10ab* double knockout (DKO) leads to decreased levels of mitochondrial proteins (Cox-IV and Samm50), increased levels of reactive oxygen species (ROS), and elevated cell death in the brain region, as shown by TUNEL staining. The snx10ab DKO-mediated cell death can be rescued by treatment with the antioxidant NAC, suggesting that Snx10 modulates piecemeal mitophagy to limit oxidative stress and maintain mitochondrial homeostasis.

Figure 1

A

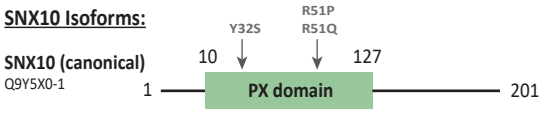

B

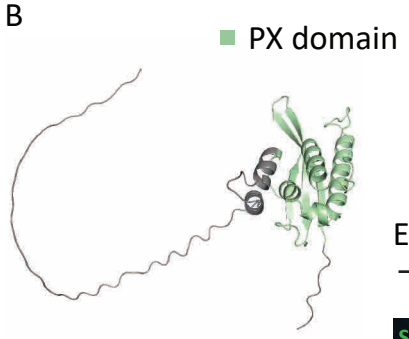

C

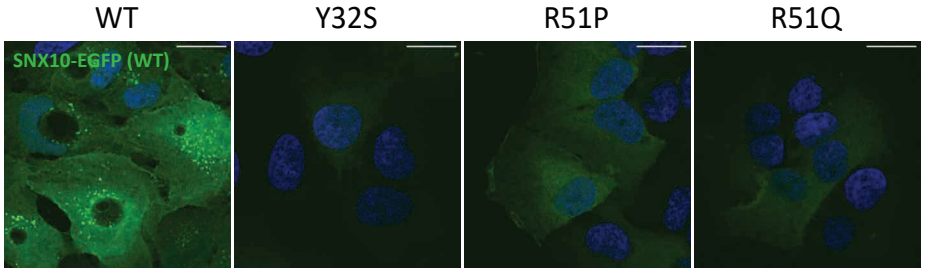

D

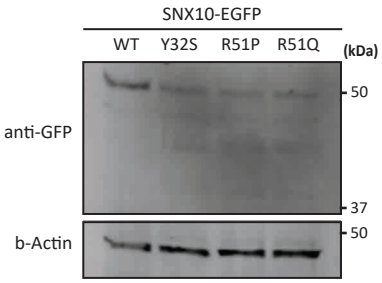

E

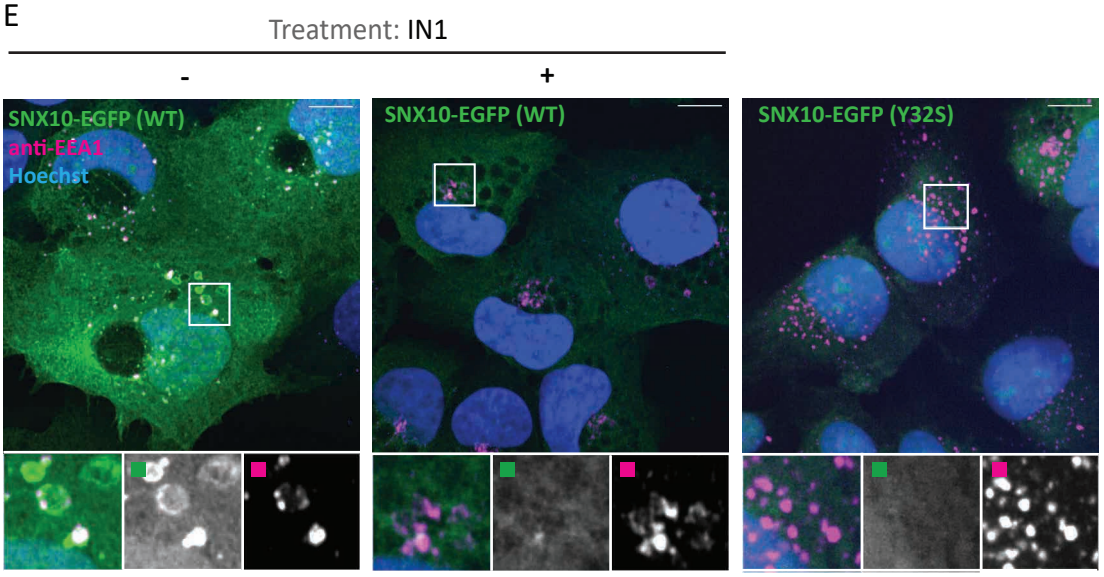

F

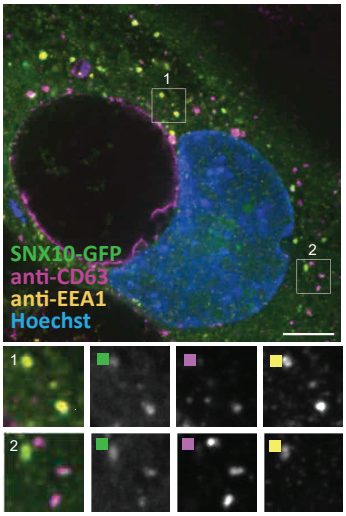

G

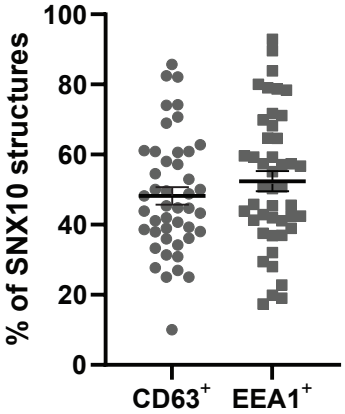

H

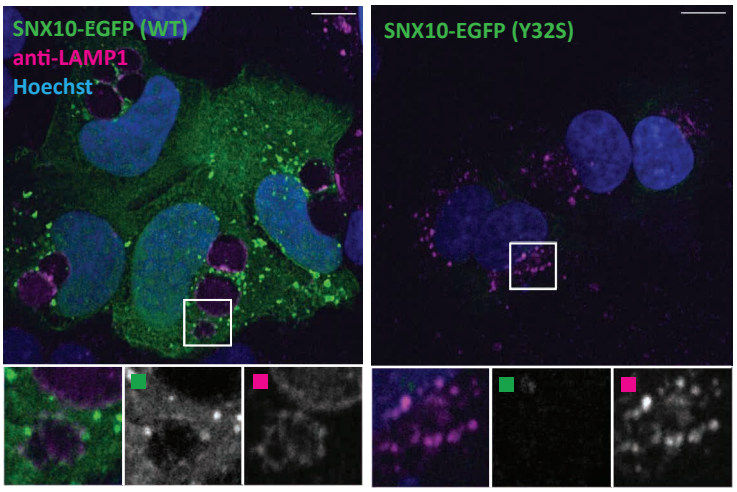

I

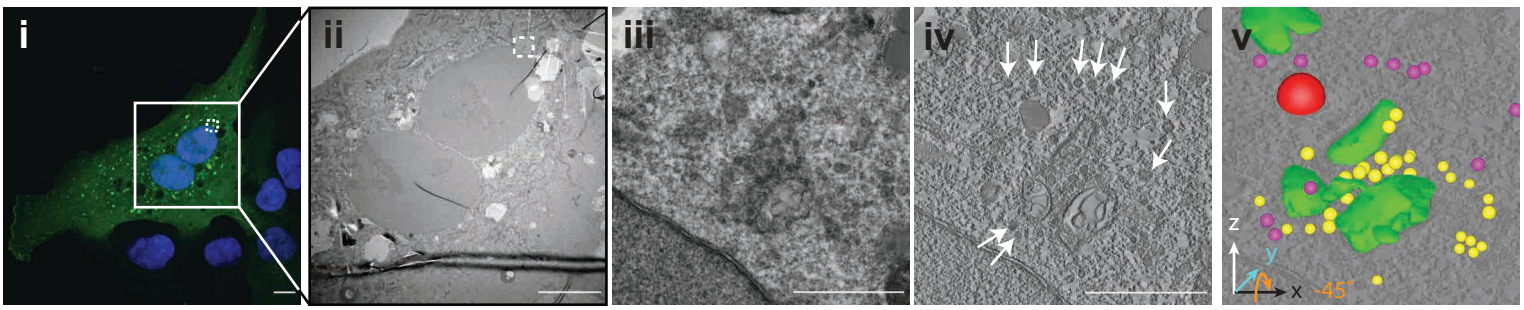

White arrows:
clathrin coated vesicles

Green: endosomes
Red: lipid droplet
Yellow: vesicles
Pink: clathrin coated vesicles

Figure 2

A

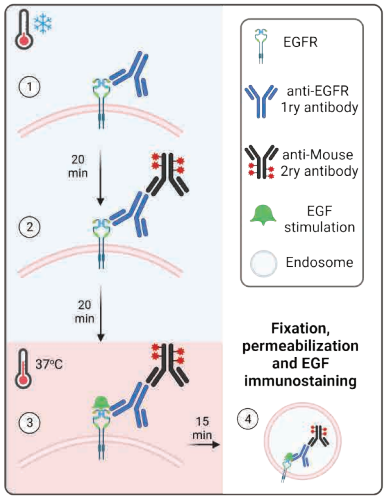

B

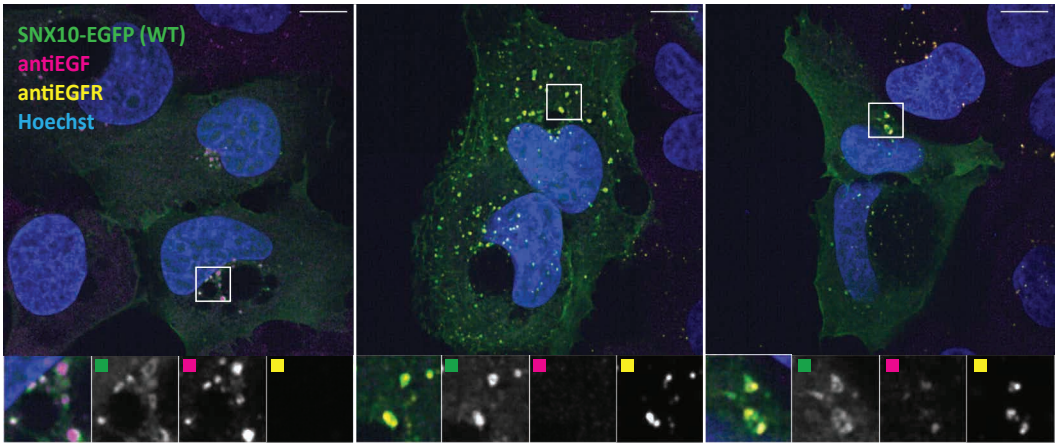

C

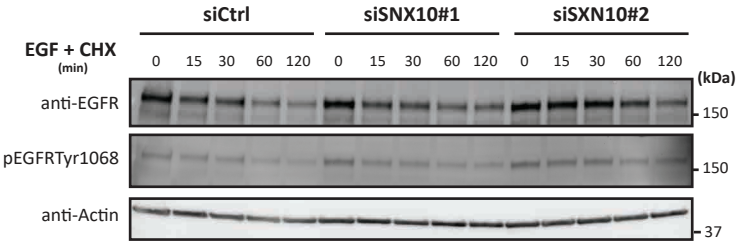

D

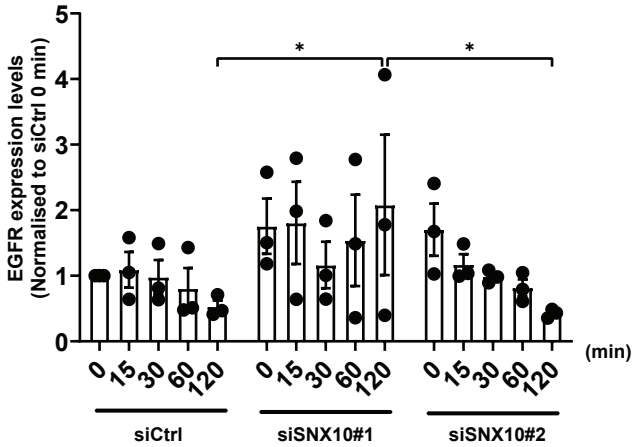

E

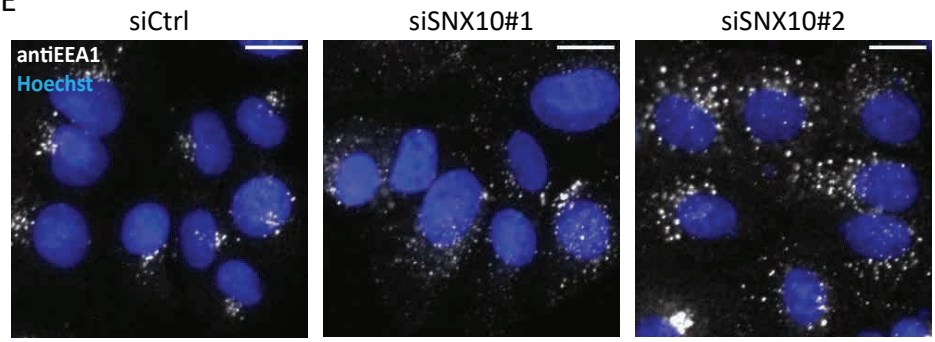

F

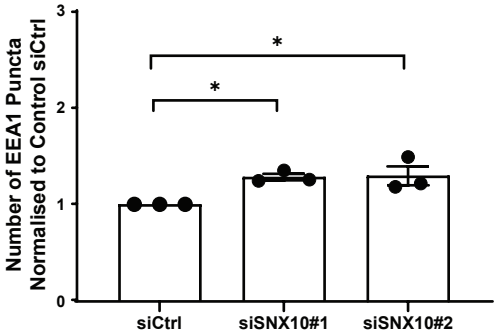

G

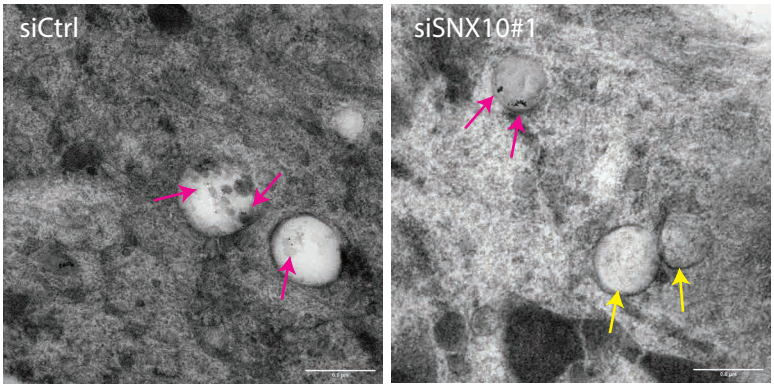

H

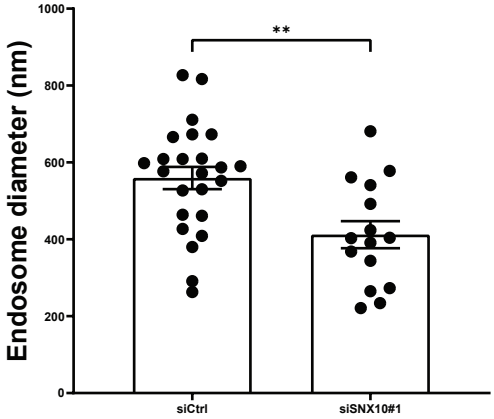

Figure 3

A

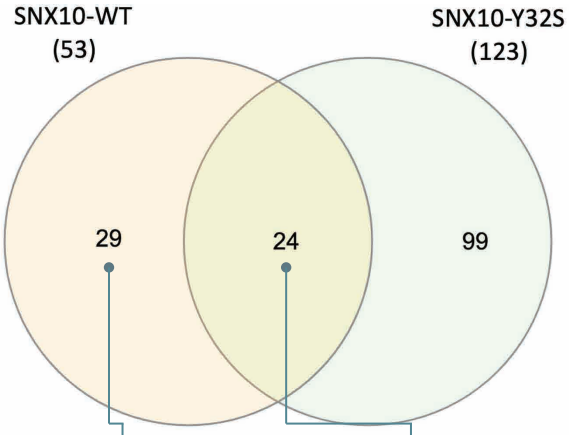

ATP5J	GNAO1	SEC24B
ATPIF1	IGHV3-38	SERPINH1
C10orf35	LAMTOR1	SPCS2
CTBP2	MVB12A	SPTLC2
DLST	NUBP1	SUCLG1
EEF1B2	PTGES2	TMA7
EEF1G	RBBP4	U2AF1
EIF3C	RBM22	UQCRFS1
EPB41L3	RCN1	VARS
GBA	RPL9	

ACTA1	MRPS36	TMEM109
CAPRIN1	RPL37A	YBX1
CAPZA2	RPS29	YBX3
CCDC47	SET	YWHAG
COX-IV	SFPQ	
EIF4B	SLC25A6	
EZR	SNX10	
GOSR1	SQSTM1	
HNRNPDL	TECR	
HSPA1A	TIGAR	

B

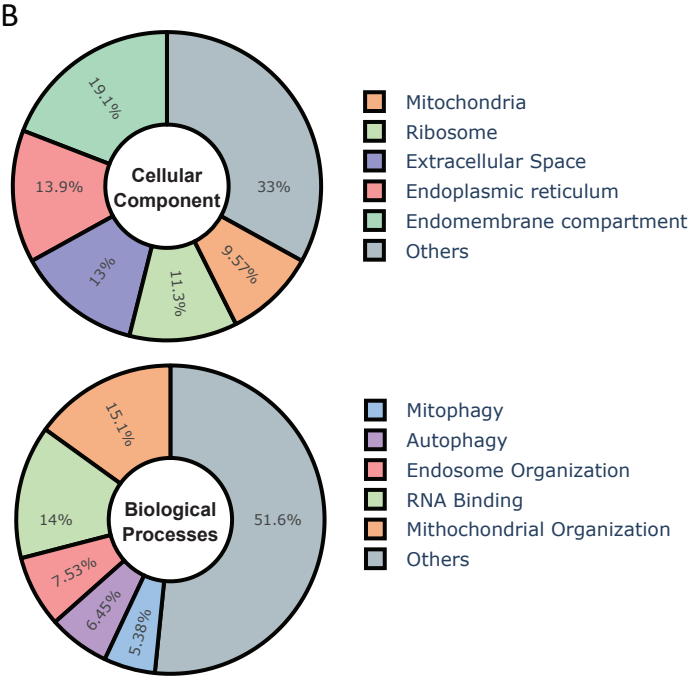

C

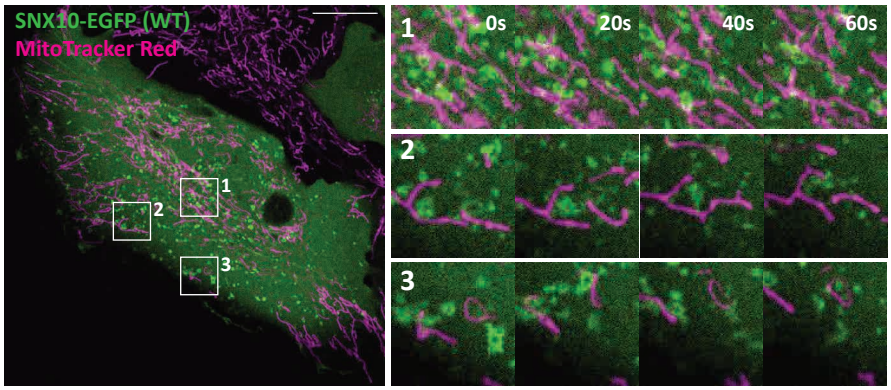

D

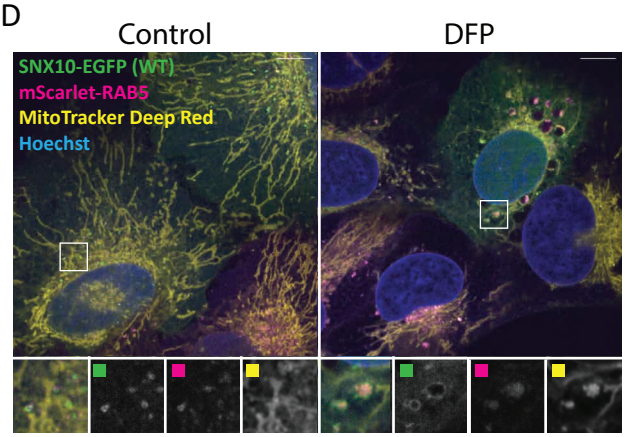

E

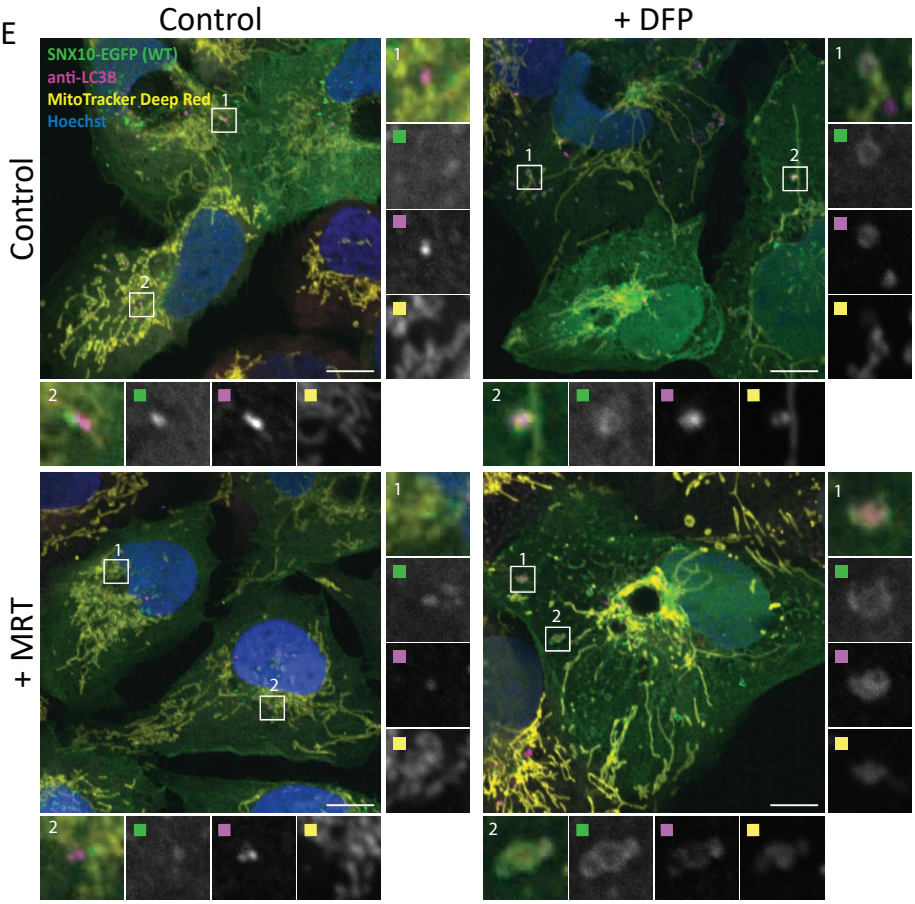

F

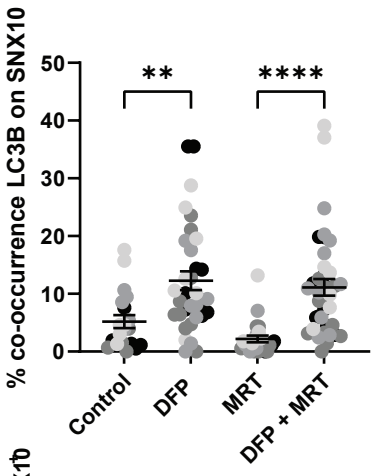

G

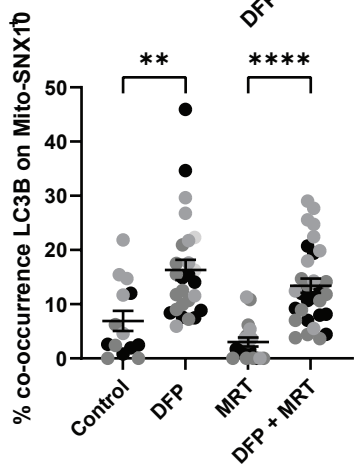

Figure 4

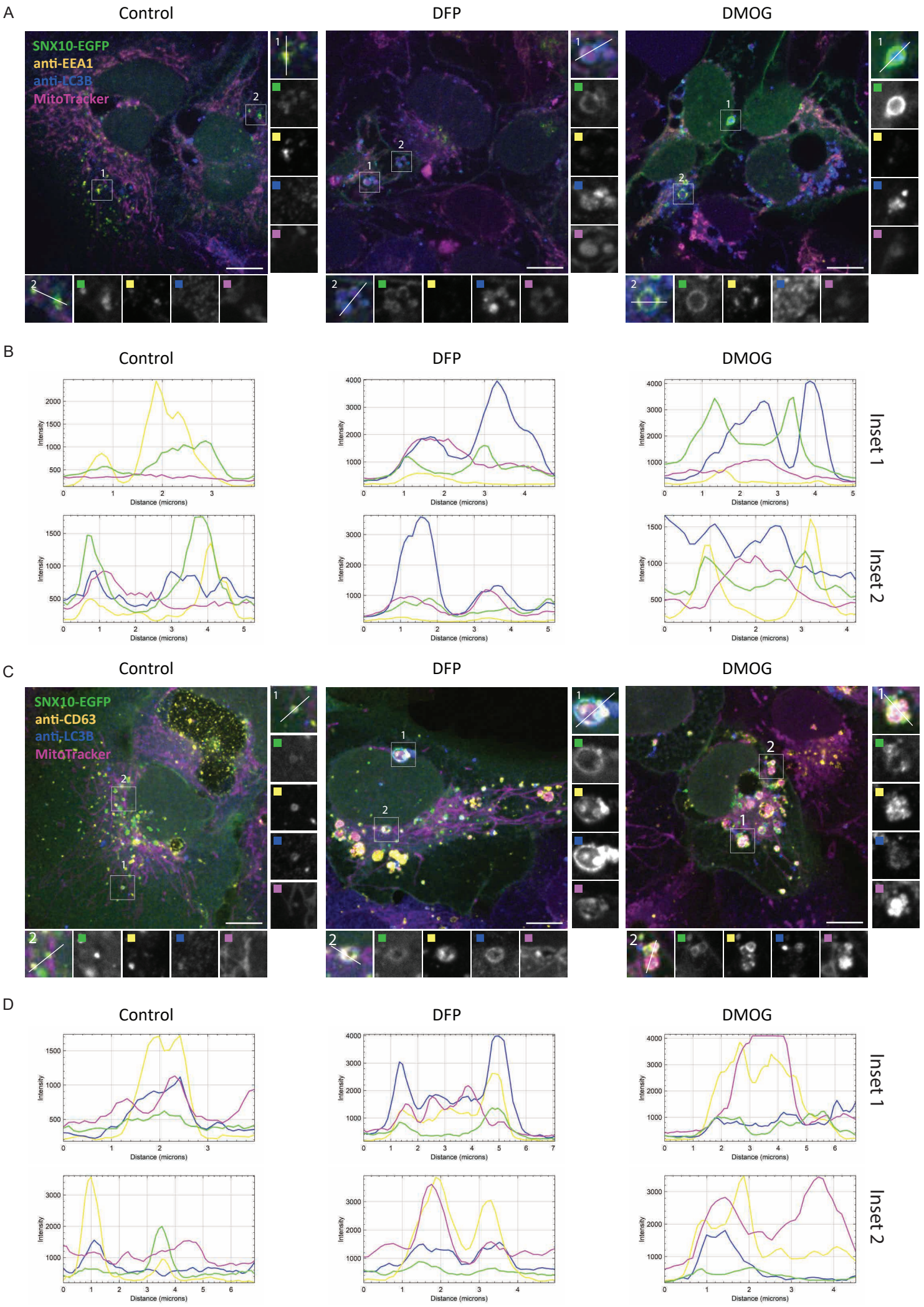
A
Control
DFP
DMOG
SNX10-EGFP
anti-EEA1
anti-LC3B
MitoTracker
B
Control
DFP
DMOG
Inset 1
Inset 2
Intensity
Distance (microns)
C
Control
DFP
DMOG
SNX10-EGFP
anti-CD63
anti-LC3B
MitoTracker
D
Control
DFP
DMOG
Inset 1
Inset 2
Intensity
Distance (microns)

Figure 5

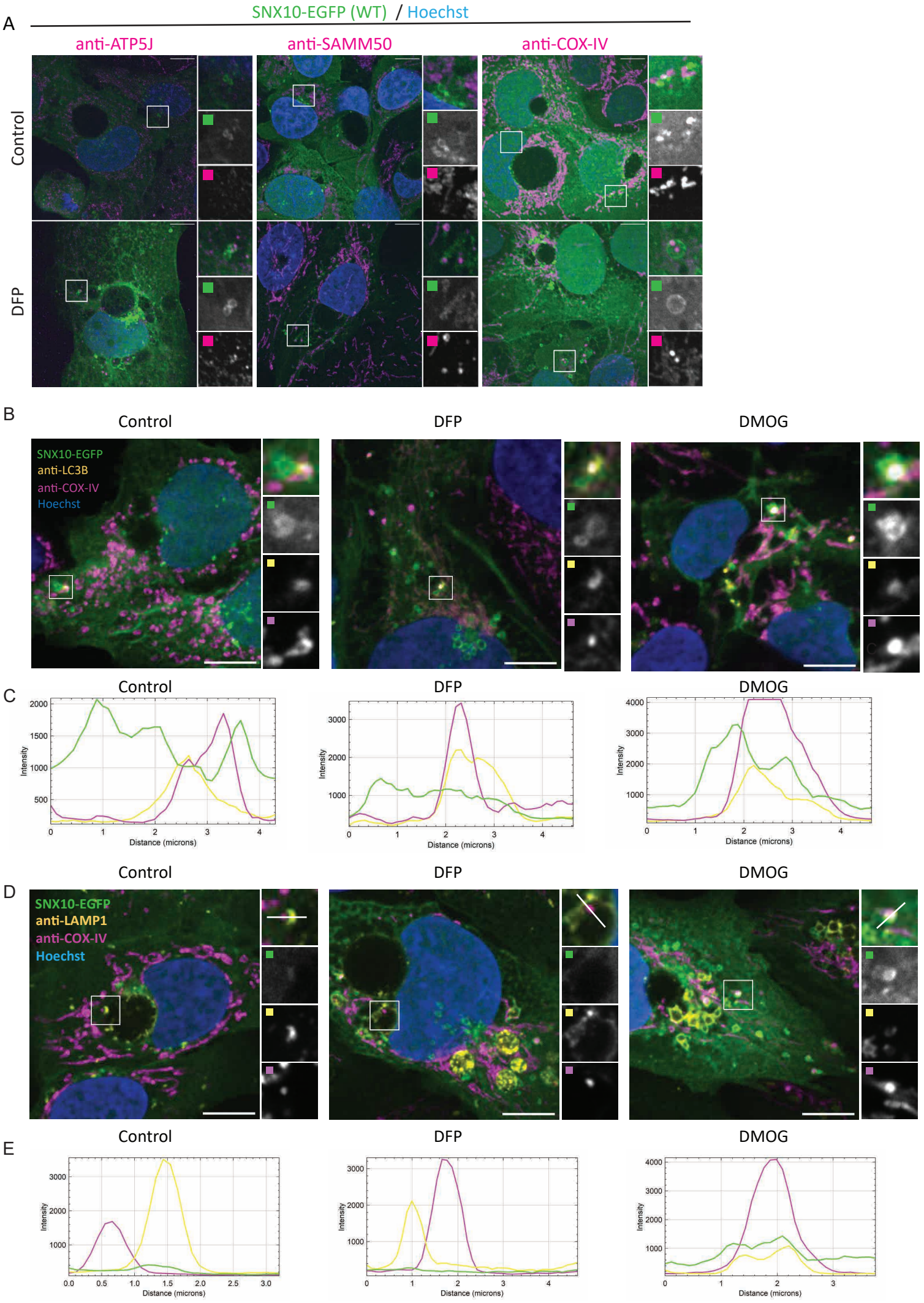
A
SNX10-EGFP (WT) / Hoechst
anti-ATP5J
anti-SAMM50
anti-COX-IV
Control
DFP
B
Control
DFP
DMOG
SNX10-EGFP
anti-LC3B
anti-COX-IV
Hoechst
C
Control
DFP
DMOG
Intensity
Distance (microns)
D
Control
DFP
DMOG
SNX10-EGFP
anti-LAMP1
anti-COX-IV
Hoechst
E
Control
DFP
DMOG
Intensity
Distance (microns)

Figure 6

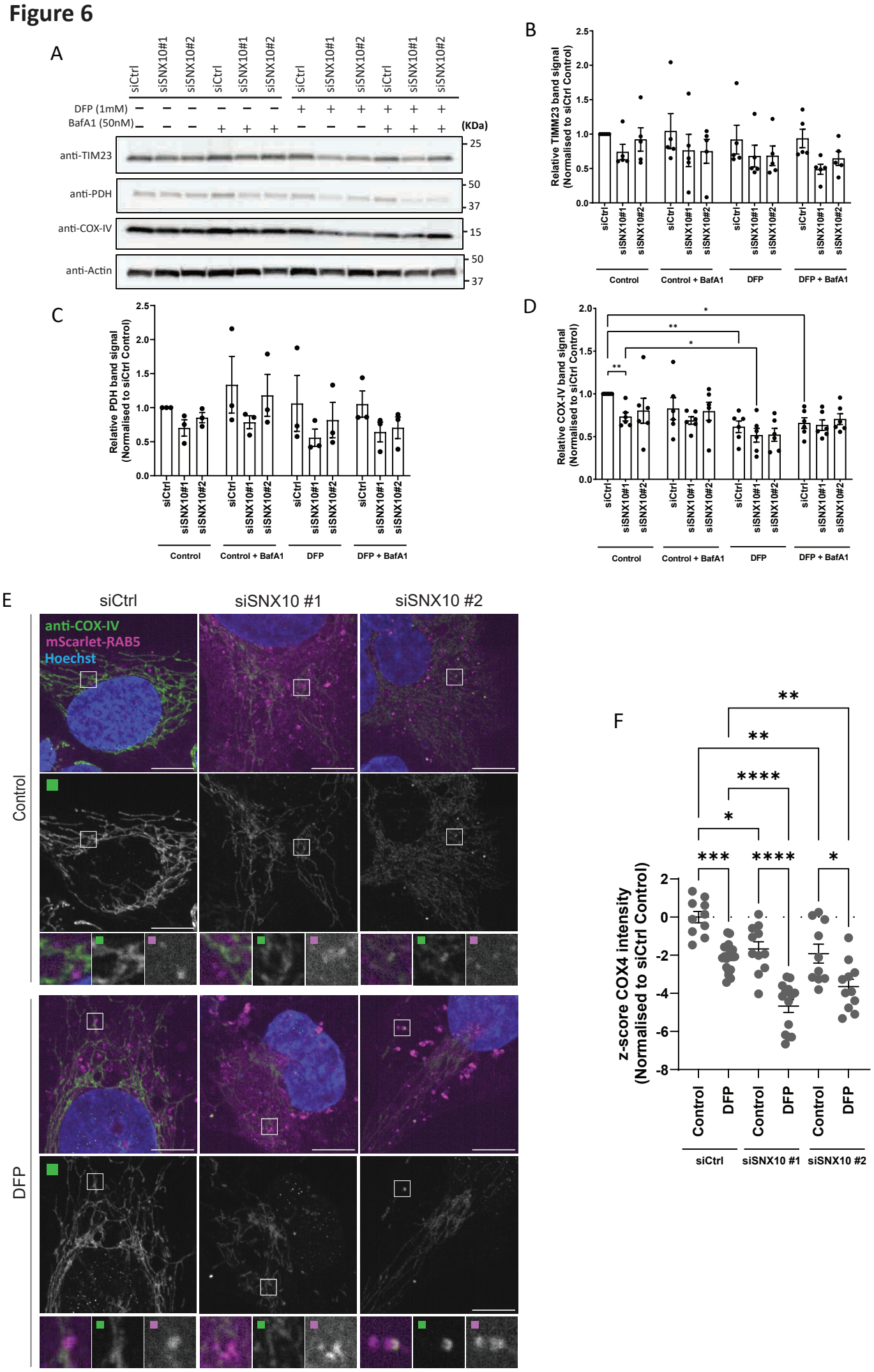
A
siCtrl
siSNX10#1
siSNX10#2
DFP (1mM)
BafA1 (50nM)
(KDa)
anti-TIM23
anti-PDH
anti-COX-IV
anti-Actin
25
50
37
15
B
Relative TIMM23 band signal (Normalised to siCtrl Control)
Control
Control + BafA1
DFP
DFP + BafA1
C
Relative PDH band signal (Normalised to siCtrl Control)
D
Relative COX-IV band signal (Normalised to siCtrl Control)
E
siCtrl
siSNX10 #1
siSNX10 #2
anti-COX-IV
mScarlet-RAB5
Hoechst
Control
DFP
F
z-score COX4 intensity (Normalised to siCtrl Control)

Figure 7

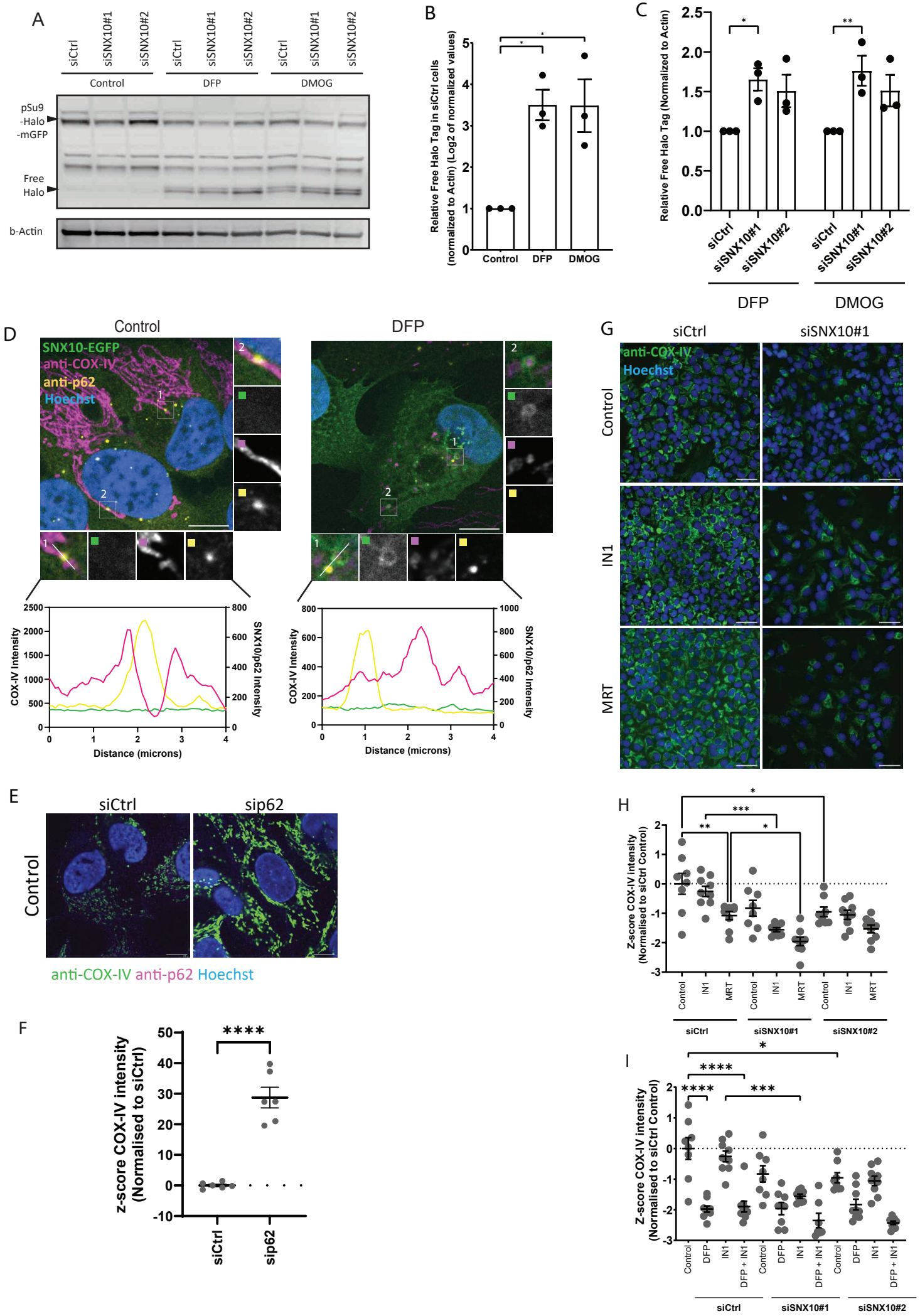
A
siCtrl
siSNX10#1
siSNX10#2
Control
DFP
DMOG
pSu9
-Halo
-mGFP
Free
Halo
b-Actin
B
Relative Free Halo Tag in siCtrl cells
(normalized to Actin) (Log2 of normalized values)
Control
DFP
DMOG
C
Relative Free Halo Tag (Normalized to Actin)
siCtrl
siSNX10#1
siSNX10#2
DFP
DMOG
D
Control
DFP
SNX10-EGFP
anti-COX-IV
anti-p62
Hoechst
COX-IV Intensity
SNX10/p62 Intensity
Distance (microns)
G
siCtrl
siSNX10#1
anti-COX-IV
Hoechst
Control
IN1
MRT
E
siCtrl
sip62
Control
anti-COX-IV anti-p62 Hoechst
F
z-score COX-IV intensity
(Normalised to siCtrl)
siCtrl
sip62
H
Z-score COX-IV intensity
(Normalised to siCtrl Control)
Control
IN1
MRT
siCtrl
siSNX10#1
siSNX10#2
I
Z-score COX-IV intensity
(Normalised to siCtrl Control)
Control
DFP
IN1
DFP + IN1
siCtrl
siSNX10#1
siSNX10#2

Figure 8

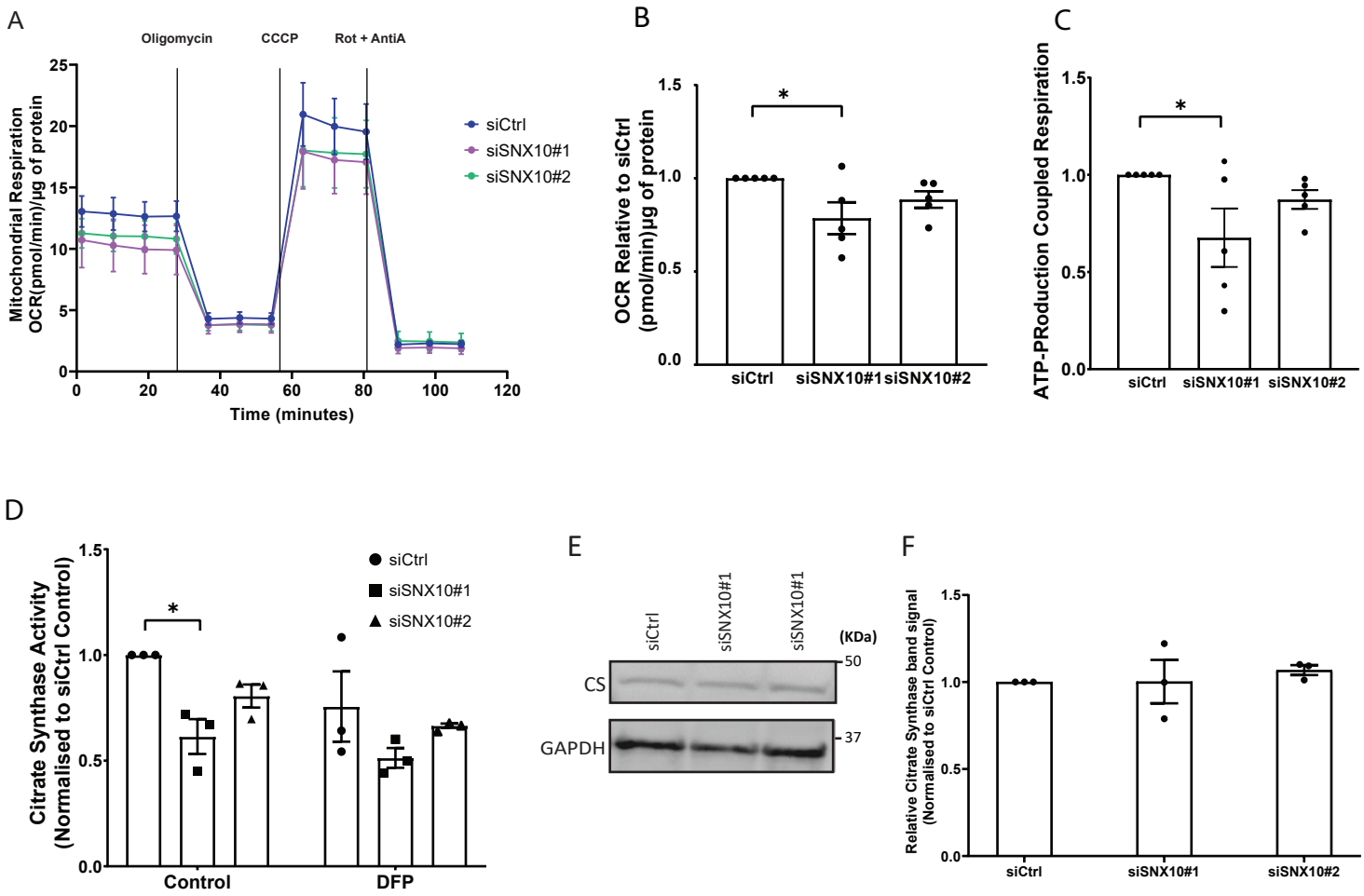
A
Oligomycin
CCCP
Rot + AntiA
Mitochondrial Respiration OCR(pmol/min)/µg of protein
Time (minutes)
siCtrl
siSNX10#1
siSNX10#2
B
OCR Relative to siCtrl (pmol/min)µg of protein
siCtrl
siSNX10#1
siSNX10#2
C
ATP-PRoduction Coupled Respiration
siCtrl
siSNX10#1
siSNX10#2
D
Citrate Synthase Activity (Normalised to siCtrl Control)
siCtrl
siSNX10#1
siSNX10#2
Control
DFP
E
siCtrl
siSNX10#1
siSNX10#1
(KDa)
CS
GAPDH
50
37
F
Relative Citrate Synthase band signal (Normalised to siCtrl Control)
siCtrl
siSNX10#1
siSNX10#2

Figure 9

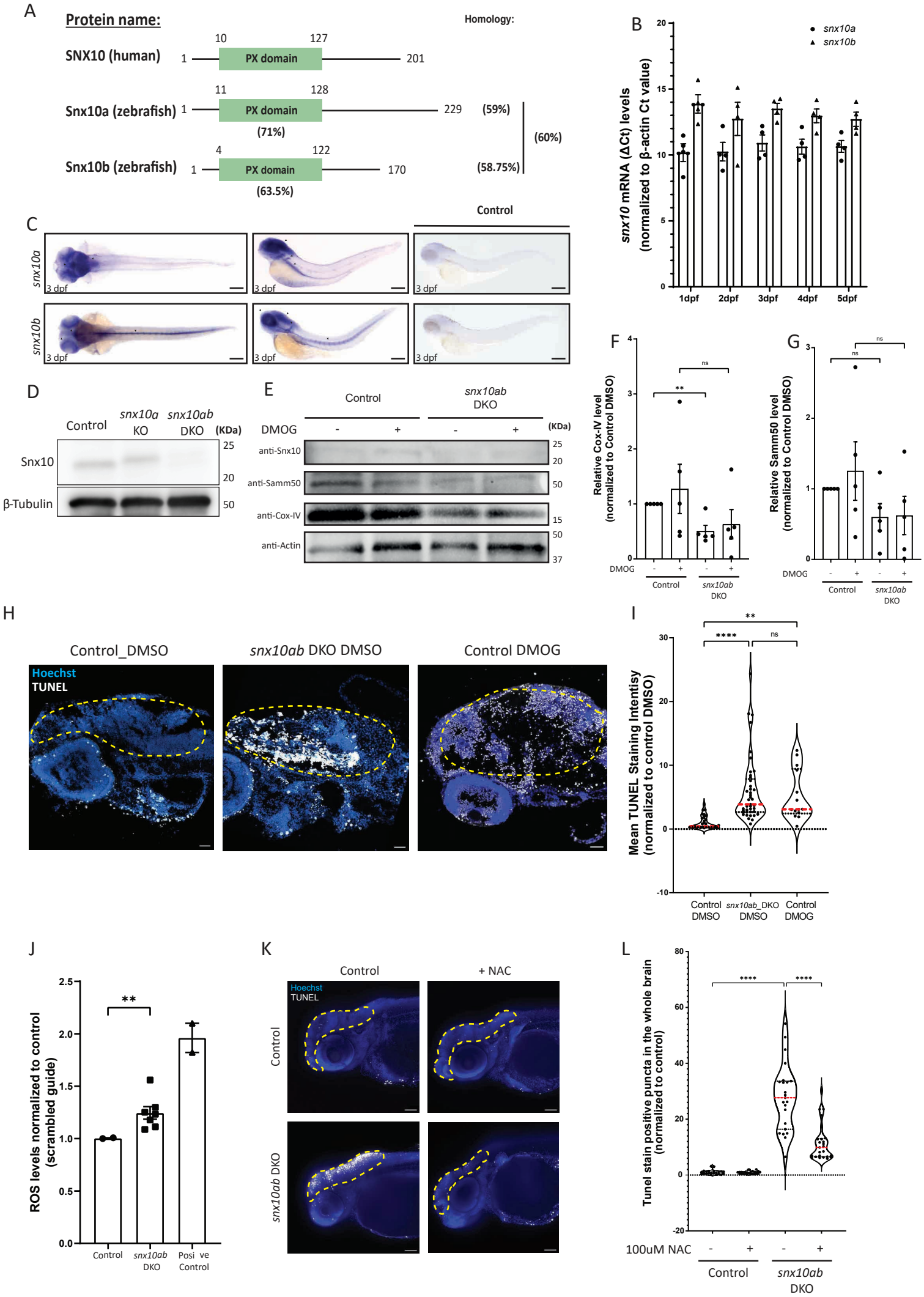
A
Protein name:
Homology:
SNX10 (human)
1
10
127
PX domain
201
Snx10a (zebrafish)
1
11
128
PX domain
229
(59%)
(71%)
(60%)
Snx10b (zebrafish)
1
4
122
PX domain
170
(58.75%)
(63.5%)
B
snx10a
snx10b
snx10 mRNA (ΔCt) levels
(normalized to β-actin Ct value)
1dpf
2dpf
3dpf
4dpf
5dpf
C
Control
snx10a
snx10b
3 dpf
D
Control
snx10a KO
snx10ab DKO
(KDa)
Snx10
β-Tubulin
25
20
50
E
Control
snx10ab DKO
DMOG
(KDa)
anti-Snx10
anti-Samm50
anti-Cox-IV
anti-Actin
F
Relative Cox-IV level
(normalized to Control DMSO)
ns
**
DMOG
Control
snx10ab DKO
G
Relative Samm50 level
(normalized to Control DMSO)
ns
ns
H
Control_DMSO
snx10ab DKO DMSO
Control DMOG
Hoechst
TUNEL
I
Mean TUNEL Staining Intentisy
(normalized to control DMSO)
**
****
ns
Control DMSO
snx10ab_DKO DMSO
Control DMOG
J
ROS levels normalized to control
(scrambled guide)
**
Control
snx10ab DKO
Posi ve Control
K
Control
+ NAC
Hoechst
TUNEL
Control
snx10ab DKO
L
Tunel stain positive puncta in the whole brain
(normalized to control)
****
****
100uM NAC
Control
snx10ab DKO

Figure 10

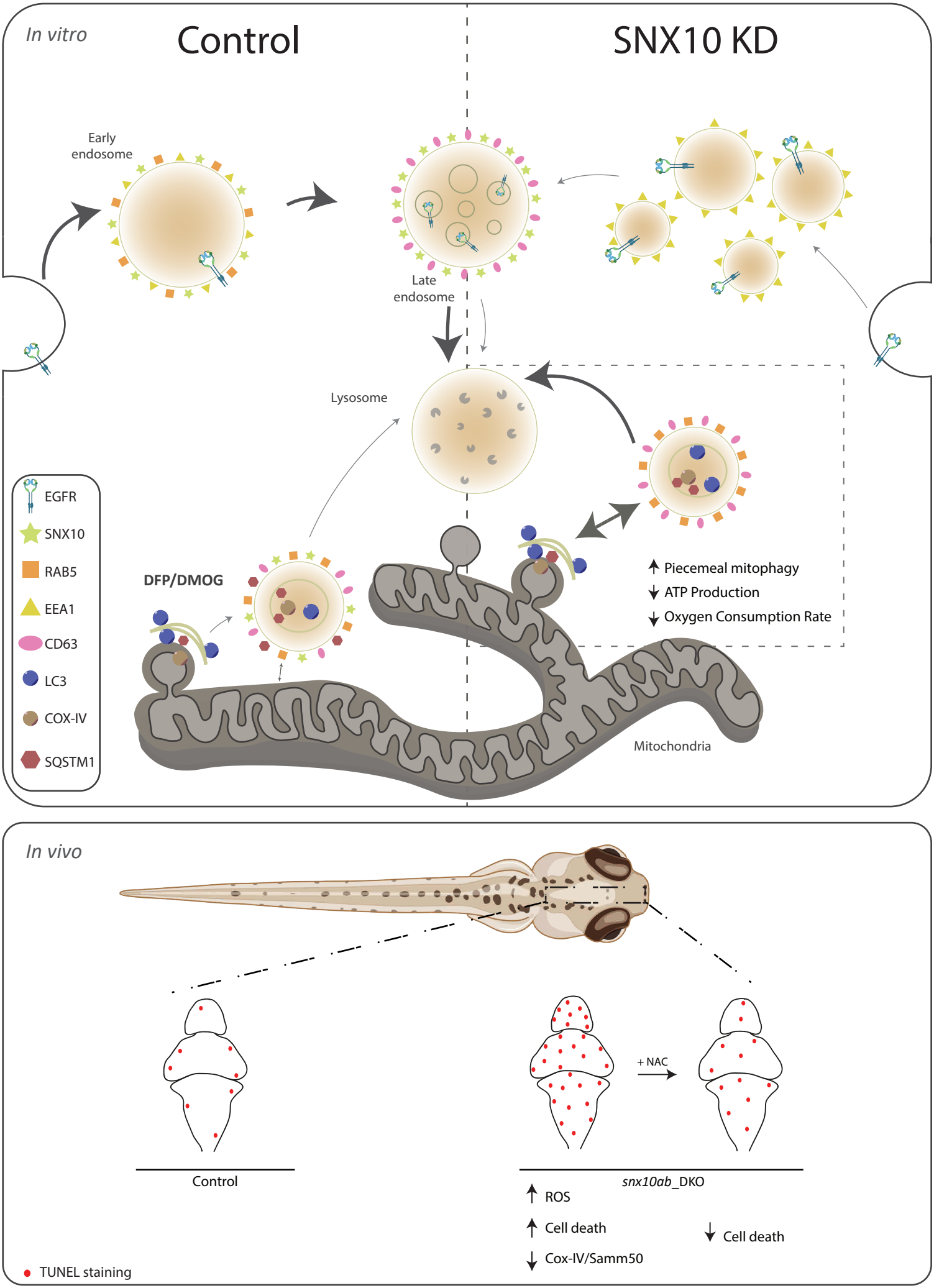
In vitro
Control
SNX10 KD
Early endosome
Late endosome
Lysosome
EGFR
SNX10
RAB5
EEA1
CD63
LC3
COX-IV
SQSTM1
DFP/DMOG
Piecemeal mitophagy
ATP Production
Oxygen Consumption Rate
Mitochondria
In vivo
+ NAC
Control
snx10ab_DKO
ROS
Cell death
Cox-IV/Samm50
Cell death
TUNEL staining